OPAL Physics Note PN308
August 13, 1997.

Limits on anomalous γWW couplings from single W production in e^+e^- collisions at $\sqrt{s} = 161 - 172$ GeV

The OPAL Collaboration

Abstract

This note describes the selection of events of the type $e^+e^- \to W^+e^-\overline{\nu}_e$ in e^+e^- collisions at $\sqrt{s} = 161 - 172$ GeV. The signal consists of final states with large missing energy and two hadronic jets or a single lepton. The cross section for this process provides a direct measurement of the couplings between a photon and two W bosons. From the data we obtain the following 95% confidence level constraints on the couplings at the γWW vertex: $|\kappa_\gamma| \leq 2.6$ and $|\lambda_\gamma| \leq 3.1$.

This note describes preliminary OPAL results to be submitted to the International Europhysics Conference on High Energy Physics, Jerusalem, 19-26 August 1997.

1 Introduction

Production of a single on-shell W boson in e^+e^- collisions involves the fusion of a virtual W and a photon exchanged in the t–channel. This reaction is interesting for the measurement of triple gauge boson couplings (TGCs) [1] and as background in the search for the Higgs boson and particles appearing in extensions of the Standard Model.

The measurement of triple gauge boson couplings (TGCs) is one of the goals of the LEP2 experimental program [2]. Whereas the couplings of fermions to the Z^0 have been precisely measured at LEP1, the couplings at the γWW and Z^0WW vertices are poorly constrained from an experimental point of view. To disentangle the relative contribution of the γWW and Z^0WW vertices to the W^+W^- production cross section in e^+e^- collisions and to set limits on possible anomalous couplings, it is necessary to study the differential cross section as a function of the $W^\pm$ production angle and the helicity state of the W bosons. Given the limited statistics available, constraints are used which relate the couplings at the γWW vertex to those at the Z^0WW vertex [3]. Single W production is instead directly sensitive to the value of the couplings at the γWW vertex [1].

Single W production leads to peculiar event topologies such as acoplanar jets or single leptons together with large missing momentum. These are the signatures often ascribed to production of new particles. A measurement of the single W cross section would then provide a check of the Monte Carlo programs used to estimate the backgrounds to the possible signals of production of new particles.

In this note we present a selection of events of the $e^+e^- \to W^+e^-\overline{\nu}_e$[1] type followed by the decays of the W boson into electrons, muons and jet pairs. Using the dependence of the cross section on the couplings at the γWW vertex we derive limits on the TGC parameters κ_γ and λ_γ. These are related to the W magnetic dipole moment (μ_W) and electric quadrupole moment (q_W) through the relations:

$$\begin{aligned} \mu_W &= \frac{e}{2M_W}(1+\kappa_\gamma+\lambda_\gamma), \\ q_W &= \frac{-e}{2M_W}(\kappa_\gamma-\lambda_\gamma). \end{aligned}$$

In the Standard Model these coupling have the values $\kappa_\gamma = 1$ and $\lambda_\gamma = 0$.

2 The single W cross section.

The two diagrams describing the production of a single W boson in e^+e^- collisions are shown in figures 1a and 1b: only the first one ($\gamma W^* \to W$ scattering) is sensitive to anomalous couplings at the γWW vertex. To create the W mass one of the two intermediate bosons must have a large momentum transfer Q^2, and the lepton coming from the corresponding vertex is therefore emitted at large angles. To avoid suppression from the W propagator, this happens for the intermediate state W. As a consequence the neutrino is emitted at large angle. The photon is instead quasi–real ($Q^2 \approx 0$), and the corresponding electron is scattered at small angles. Therefore signatures for single W events are either an isolated lepton or a pair of jets originating from the decay of the W, accompanied by a large missing transverse momentum and a final state electron lost in the beam pipe. Contributions from diagrams where the intermediate photon is replaced by a Z^0 boson are negligible at the current energies, since both the Z^0 and the W boson would have to be far off the mass shell. Hence the single W reaction is much less sensitive to the couplings at the Z^0WW vertex.

This picture is complicated by the interference with other diagrams leading to the same four–fermion final state. Two other categories of events must be considered: the doubly resonant process resulting in pair production of W bosons (the CC03 diagrams) and the charged current deep inelastic scattering process (shown in figure 1c) giving non–resonant final states. The contribution from these

[1] Charge conjugation is implied throughout this note.

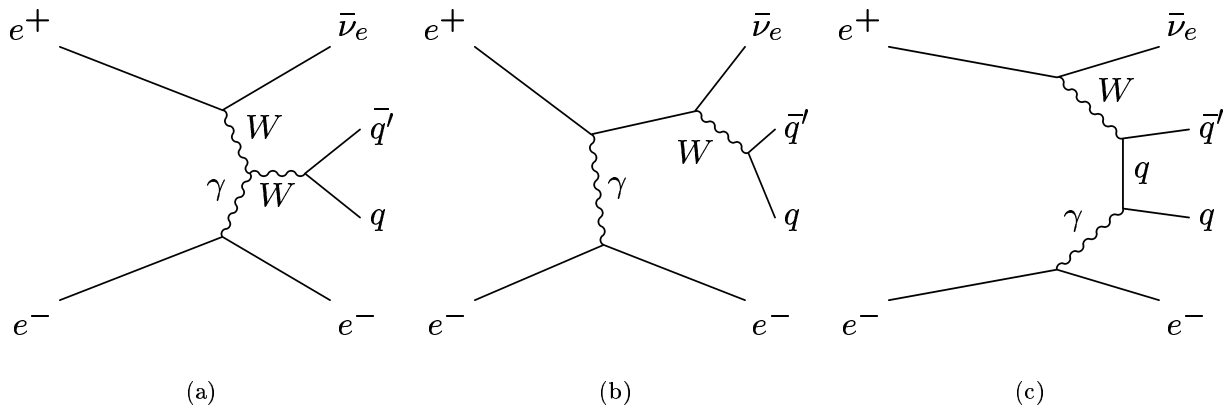

Figure 1: The diagrams (a,b) dominating the $e^+e^- \to q\overline{q}'e\overline{\nu}_e$ final state in the signal region of the phase space and the diagram giving non–resonant final states (c).

processes can be suppressed by kinematic cuts. A cut on the polar angle[2] of the outgoing electron selects t–channel photon exchange and reduces the contribution from W pair production. A cut on the energy or the invariant mass of the W decay products reduces the contribution from non–resonant processes. Four–fermion events which do not satisfy these criteria are regarded as background. The differential cross sections with respect to the incoming electron direction and to the invariant mass of the jet pair for the $e^+e^- \to u\overline{d}e\overline{\nu}_e$ reaction predicted by the `grc4f` [4] program are shown in figure 2. The contributions of the two dominating diagrams in the signal phase space region cannot be separated, as they give similar kinematical distributions and their amplitudes interfere destructively.

For the $q\overline{q}'e\overline{\nu}_e$ final state we adopt in this note the following definition of the single W signal:

- $\theta_e < 100$ mrad, where θ_e is the polar angle of the forward emitted electron,
- $|\cos\theta_q|, |\cos\theta_{\overline{q}'}| < 0.98$, where $\theta_q, \theta_{\overline{q}'}$ are the polar angles of the quarks coming from the W decay, and
- $70 < M_{q\overline{q}'} < 90$ GeV/c^2, where $M_{q\overline{q}'}$ is the invariant mass of the quark pair.

Summing the cross section for the $e^+e^- \to u\overline{d}e\overline{\nu}_e$ and $e^+e^- \to c\overline{s}e\overline{\nu}_e$ processes and neglecting quark mixing we obtain a prediction for the single W production cross section followed by its hadronic decay of 150 fb at $\sqrt{s} = 161$ GeV and 205 fb at $\sqrt{s} = 172$ GeV.

For the $\ell\nu_\ell e\overline{\nu}_e$ final state we use the following definition of the single W signal:

- $\theta_e < 35$ mrad,
- $|\cos\theta_\ell| < 0.95$, where θ_ℓ is the angle of the charged lepton coming from the W decay,
- $E_e > 30$ GeV or $E_\mu > 20$ GeV, where E_ℓ is the energy of the lepton coming from the W decay. The harder cut is applied to electrons from $W \to e\overline{\nu}_e$ to reject additional non–resonant t–channel contributions to this final state.

With these cuts, cross sections of approximately 25 and 30 fb are predicted for the leptonic channels at $\sqrt{s} = 161$ and 172 GeV respectively[3].

[2] A right-handed coordinate system is adopted, where the x–axis points to the centre of the LEP ring, and positive z is along the electron beam direction. The angles θ and ϕ are the polar and azimuthal angles, respectively.

[3] The predicted cross section for the hadronic channel applying the angular ($|\cos\theta_q| < 0.95$) and an energy cut ($E_q > 20$ GeV) to both quarks is approximately 130 and 170 fb at $\sqrt{s} = 161$ and 172 GeV respectively.

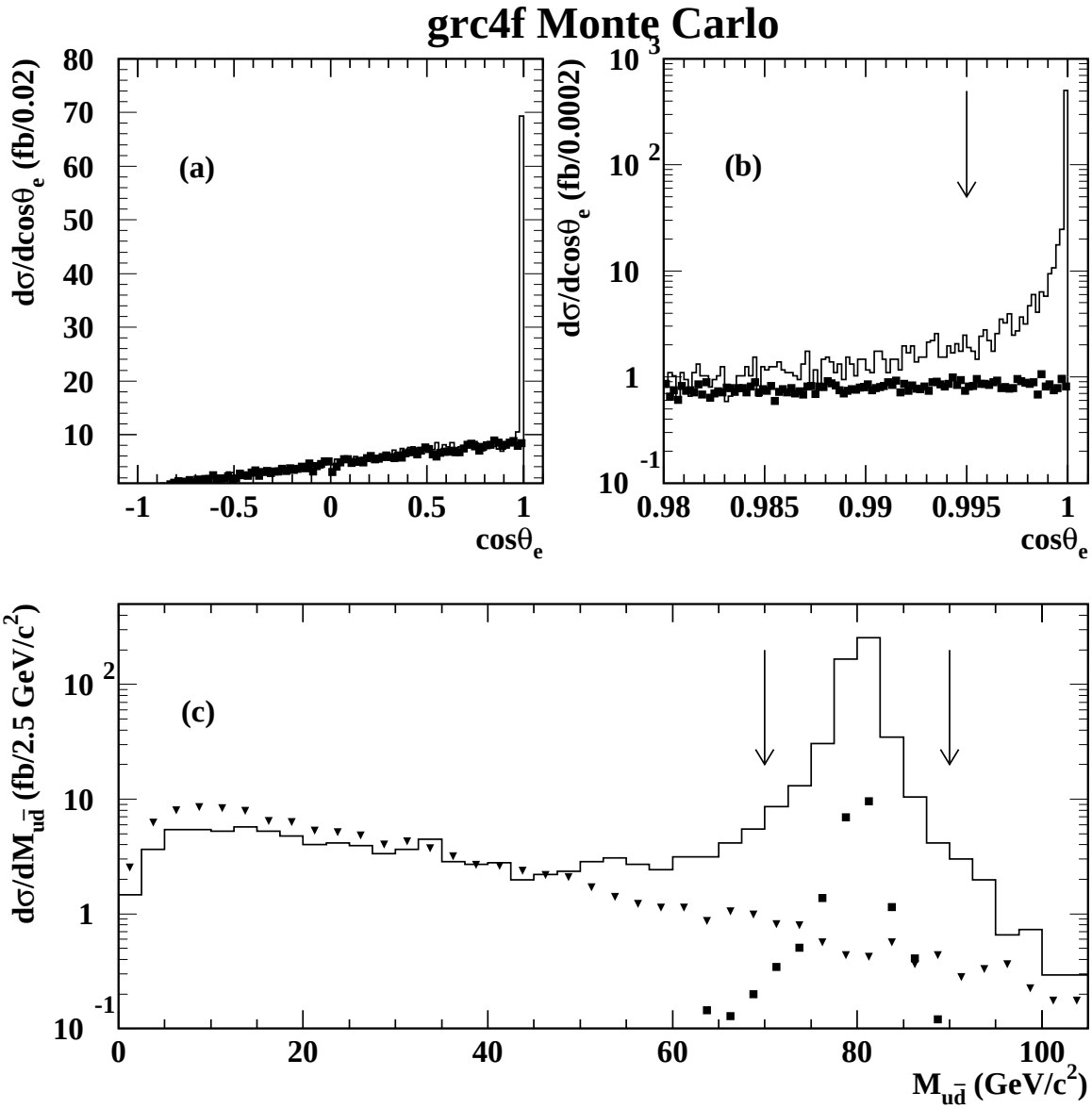

Figure 2: Differential cross section for the $e^+e^- \to u\bar{d}e\bar{\nu}_e$ process at $\sqrt{s} = 172$ GeV predicted by `grc4f`. In (a) and (b) we show the angular distribution of the electron prior to any cuts: the open histogram shows the cross section calculated including all the diagrams and the squares only the CC03 diagrams. A clear excess at $\cos\theta_e \approx 1$ is seen in the first case. In (c) we show the invariant mass of the two quarks for $\cos\theta_e > 0.995$. The open histogram shows the cross section calculated including all diagrams, while the triangles indicate the contribution from non–resonating diagrams. The squares show the residual contribution of the CC03 cross section. The cuts defining the single W signal are indicated by the arrows.

With these definitions the single W cross section is approximately 4 and 9 times smaller than the CC03 cross section for the same four–fermion final states at the two centre-of-mass energies.

Since the anomalous couplings κ_γ and λ_γ enter linearly in the Lagrangian that describes the γWW vertex, the cross section depends quadratically on the values of the TGCs. The parameters of this quadratic function are similar for all the decay channels of the W boson, with the exception of the electronic channel, due to the additional contributions to the $e^+\nu_e e^-\overline{\nu}_e$ final state from neutral current processes and the different cuts used to define the signal.

3 Data and Monte Carlo samples

The OPAL detector, described in detail in ref. [5], is a multipurpose apparatus having nearly complete solid angle coverage. The central detector consists of a silicon strip detector and tracking chambers, providing charged particle tracking for over 96% of the full solid angle, inside a uniform solenoidal magnetic field of 0.435 T. A lead-glass electromagnetic calorimeter located outside the magnet coil is hermetic in the polar angle range of $|\cos\theta| < 0.82$ for the barrel region and $0.81 < |\cos\theta| < 0.984$ for the endcap region. The magnet return yoke, consisting of barrel and endcap sections along with pole tip regions, is instrumented for hadron calorimetry in the region $|\cos\theta| < 0.99$. Four layers of muon chambers cover the outside of the hadron calorimeter. Calorimeters close to the beam axis measure the luminosity using small angle Bhabha scattering events and complete the geometrical acceptance down to 33 mrad. These include the forward detectors (FD) which are lead-scintillator sandwich calorimeters and, at smaller angles, silicon tungsten calorimeters (SW) [6] located on both sides of the interaction point. The gap between the endcap electromagnetic calorimeter and the FD is filled by an additional lead-scintillator electromagnetic calorimeter, called the gamma-catcher (GC).

For this note we analyse samples of 9.89 ± 0.06 pb^{-1} and 10.36 ± 0.06 pb^{-1} integrated luminosities collected with the OPAL detector in 1996 at the luminosity weighted centre-of-mass energies of $\sqrt{s} = 161.30 \pm 0.06$ GeV/c^2 and $\sqrt{s} = 172.12 \pm 0.06$ GeV/c^2 [7] respectively.

To study the signal efficiency we use samples of 1000 Monte Carlo events generated using the `grc4f` [4] program for each decay channel of the W boson. Hadronisation is performed by JETSET [8]. With `grc4f` we also study the dependence of the cross section and of the selection efficiency on the values of the TGCs. In the calculation of the cross section the electromagnetic coupling constant is set at $\alpha_{em} = 1/135.8$ as suggested in [9] . This value is obtained as the weighted average of $1/\alpha^2_{em}$ over the Q^2 range covered by the photon exchanged in the single W process. The change of the electromagnetic coupling only affects the total cross section, but not the kinematical distributions. It should be noted that the coupling at the production and decay vertices of the W boson involves the electromagnetic coupling at $Q^2 = M^2_{Z^0}$ through the weak coupling G_μ. Two different methods to generate initial state radiation photons are implemented in the `grc4f` Monte Carlo: the structure function method (SF) [10] and a QED parton shower method (PS) [11]. In the SF method all photons are emitted collinear to the beam direction, and therefore escape detection. In the PS method the photons are instead generated with a finite transverse momentum whose distribution is in good agreement with analytical calculations of single and double hard photon emission for s–channel processes. This method is however not so thoroughly tested for t–channel processes. It is claimed that the PS method overestimates the transverse momenta of the photons for t–channel processes such as Bhabha scattering [12]. We compute cross sections and selection efficiencies with both methods and conservatively take the absolute difference as a systematic error.

Backgrounds from processes with four–fermions in the final state are evaluated using `grc4f`, EXCALIBUR [13] and FERMISV [14]. Hadronic events produced through the $e^+e^- \to q\overline{q}(\gamma)$ process are simulated using PYTHIA [8] and HERWIG [15]. Other backgrounds involving two fermions in the final state are obtained using KORALZ [16] for $e^+e^- \to \mu^+\mu^-(\gamma)$ and $e^+e^- \to \tau^+\tau^-(\gamma)$, BHWIDE [17] and TEEGG [18] for $e^+e^- \to e^+e^-(\gamma)$, and NUNUGPV [19] for $e^+e^- \to \nu\overline{\nu}\gamma$. Photonic final states produced in the reaction $e^+e^- \to \gamma\gamma(\gamma)$ are simulated using RADCOR [20]. Backgrounds from two–photon

processes are evaluated using PYTHIA, HERWIG, PHOJET [21], TWOGEN [22] and the Vermaseren program [23]. Double counting of the $e^+e^-f\bar{f}$ final state between four–fermion and two–photon samples is avoided by separating contributions from different classes of diagrams, or by performing kinematic cuts. At least two independent Monte Carlo estimates are available for each category of two-photon and four-fermion background. All Monte Carlo samples are processed through the full simulation of the OPAL detector [24], and then subjected to the same reconstruction and analysis procedures applied to real data.

4 Hadronic final states ($q\bar{q}'e\bar{\nu}_e$)

4.1 Event selection

We select multihadronic events requiring at least 6 tracks and 8 clusters in the electromagnetic calorimeter. This cut almost completely removes events with two or four leptons in the final state. In each event two jets are then reconstructed with the Durham [25] recombination scheme using tracks and energy clusters in both the electromagnetic and the hadronic calorimeters. Only events which satisfy the cut $y_{23} < 0.03$ are considered, y_{23} being the value of the jet resolution parameter at which the event classification changes from 3 to 2 jets. This cut removes almost all $W^+W^- \to q\bar{q}'q\bar{q}'$ decays and a large fraction of the $W^+W^- \to q\bar{q}'\ell\bar{\nu}_\ell$ events where the lepton is usually reconstructed as a third well separated jet. Measured jet energies are corrected for double counting using the algorithm described in [26]. The corrected jet energies are then used to compute the missing momentum vector. Finally we require the invariant mass of the two jet system to be larger than 12 GeV/c^2 to reduce the amount of hadronic events from $\gamma\gamma$ collisions. This preselection is 80% efficient for the $e^+e^- \to q\bar{q}'e\bar{\nu}_e$ events satisfying the single W kinematic cuts, and results in samples of 2440 and 2661 events at $\sqrt{s} = 161$ and 172 GeV respectively. The expected background, its composition, the prediction for the signal efficiency and the observed number of events are given in tables 1 and 2 for $\sqrt{s} = 161$ and 172 GeV respectively.

To reject further hadronic events from $\gamma\gamma$ collisions, and to ensure that jets are well contained so that their energy and the missing momentum vector are correctly measured, we apply a veto on large energy deposits in the forward detectors (cut A). Furthermore we require that at least one jet is found at large polar angles with respect to the beam direction (cut B). To reduce radiative returns to the Z^0 we also require that the momentum of the two jet system does not point towards the beam direction. We require (cut A):

- $E_{GC} \leq 10.0$ GeV (energy deposited in the GC),
- $E_{FD} \leq 10.0$ GeV (energy deposited in the FD),
- $E_{SW} \leq 40.0$ GeV (energy deposited in the SW),

and (cut B):

- $|\cos\theta_{j_1}| + |\cos\theta_{j_2}| \leq 1.8$, with θ_{j_i} denoting the polar angle of the i^{th} jet,
- $|\cos\theta_{jj}| \leq 0.92$, θ_{jj} being the reconstructed polar direction of the two jet system.

To enhance further the single W signal we apply cuts on the missing transverse momentum and on the acoplanarity angle[4]. These cuts strongly reduce the hadronic background from the $e^+e^- \to q\bar{q}(\gamma)$ reaction and from $\gamma\gamma$ collisions. The distributions of the acoplanarity and of the missing transverse momentum are shown in figure 3 for the data and the Monte Carlo prediction of the signal and of the background. We require (cut C):

[4]The acoplanarity is defined as the complement to 180° of the angle between the two jet axes in the plane transverse to the beam axis.

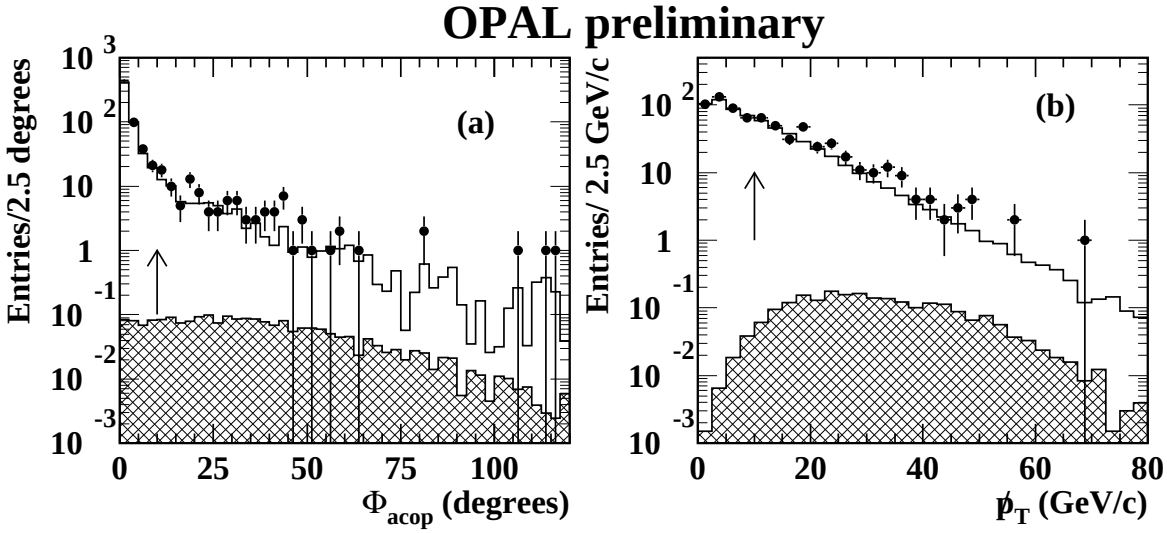

Figure 3: Acoplanarity (a) and missing transverse momentum (b) distribution for the Monte Carlo simulation (open histogram) and the 161 and 172 GeV data (full points). The contribution from the expected single W signal is shown as hatched histogram. The arrows indicate the position of the cuts.

- $\not{p}_t \geq 10.0$ GeV/c, where $\not{p}_t$ is the missing transverse momentum,
- $\phi_{\rm acop} \geq 10^\circ$, where $\phi_{\rm acop}$ is the acoplanarity angle, and
- $(\not{p}_t/1\ GeV/c)\ + 1.5(\phi_{\rm acop}/1^\circ) \geq 50$.

The remaining background is dominated by the $\rm W^+W^- \to q\overline{q}'\ell\overline{\nu}_\ell$ decays and is reduced by identifying the lepton coming from the decay of one of the W bosons, treating each track in the event as a possible candidate (events in which the lepton is emitted along the beam direction constitute a small irreducible background). In the events of this type surviving the y_{23} cut the lepton is rather close in angle to one of the hadronic jets. To have high electron and muon identification efficiency we first apply criteria best suited for isolated tracks and low multiplicity environments [27]. Then in case of failure we apply lepton identification criteria used in high multiplicity jets [28, 29]. Tracks from hadronic τ decays in $\rm W^+W^- \to q\overline{q}'\tau\overline{\nu}_\tau$ are then identified as in [30]. For each track identified as a lepton or as coming from the decay of a τ (for the 3-prong decay of the τ we construct a pseudo-track summing the momenta of the three tracks), we calculate the transverse momentum p_t^{lep} relative to the axis of the jet to which the track belongs to. Hadrons misidentified as leptons and genuine leptons produced in the semileptonic decay $\rm W \to c\overline{s} \to (e, \mu)$ have a low p_t^{lep} in contrast to the leptons coming directly from the W decay. The distribution of the maximum transverse momentum among the tracks identified as leptons in each event is shown in figure 4. After the cut $\max(p_t^{lep}) \leq 3.0$ GeV/c (cut D) the expected number of events is 2.2 (3.9) at $\sqrt{s} = 161(172)$ GeV, with an expected signal contribution of 0.68 (0.96) events. Three events are observed in the data at $\sqrt{s} = 161$ GeV and four at 172 GeV.

The remaining background is dominated by $\rm W^+W^- \to q\overline{q}'\tau\overline{\nu}_\tau$ decays. To reduce it we apply a cut on the missing energy $\not{E}$ (cut E):

- $\not{E} \geq 20.0$ GeV at $\sqrt{s} = 161$ GeV, and
- $\not{E} \geq 35.0$ GeV at $\sqrt{s} = 172$ GeV.

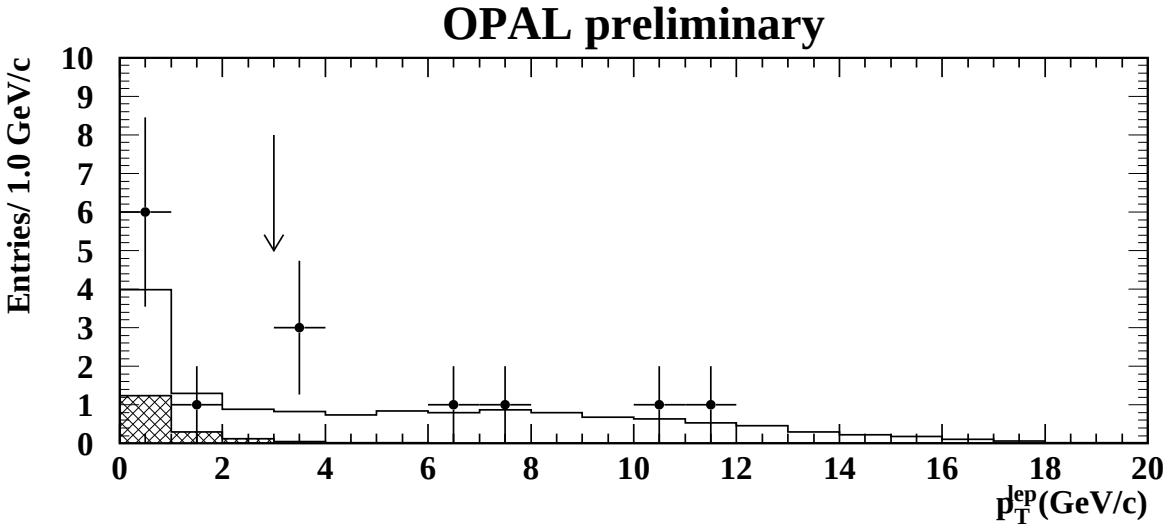

Figure 4: Distribution of the maximum transverse momentum relative to the jet axis among the tracks identified as leptons (events without leptons are recorded in the first bin of the histogram). The open histogram shows the distribution expected from the Monte Carlo simulation, and the full dots represent the 161 and 172 GeV data points. The contribution from the expected single W signal is shown as a hatched histogram. The arrow indicates the position of the cut.

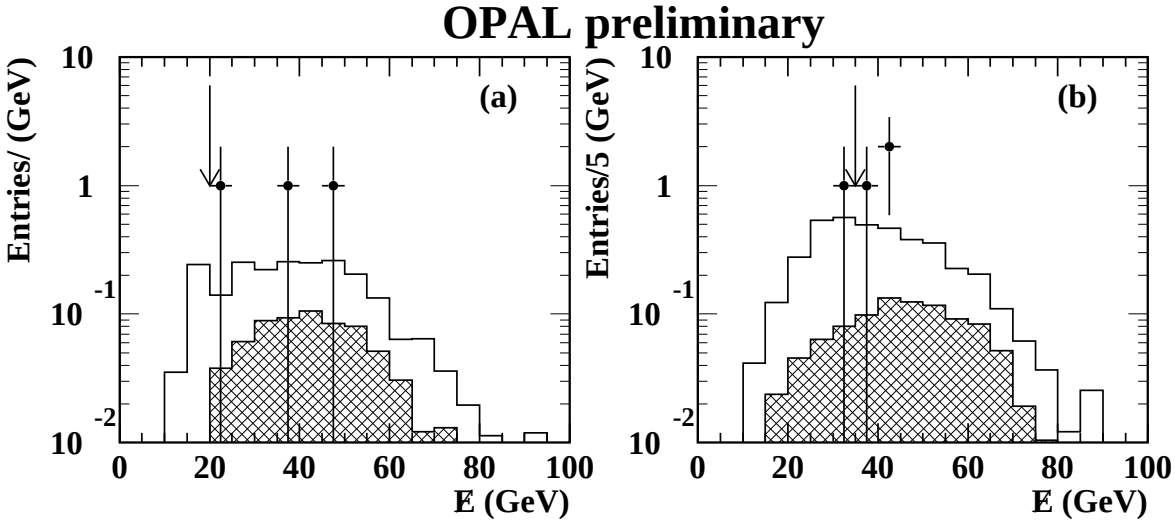

Figure 5: Distribution of the missing energy for $\sqrt{s}$ = 161 GeV (a) and 172 GeV (b). The open histogram shows the distribution expected from the Monte Carlo simulation, and the full dots represent the 161 and 172 GeV data points. The contribution from the expected single W signal is shown as hatched histogram. The arrows indicate the position of the cuts.

In single W events both the energy of the neutrino and of the forward scattered electrons are not measured. Despite the presence of two or three neutrinos in the final state, the $W^+W^- \to q\overline{q}'\tau\overline{\nu}_\tau$ events have on average a smaller missing energy compared to the single W events, as shown in figure 5. The missing energy cut has to be raised when moving to $\sqrt{s} = 172$ GeV away from the W^+W^- production threshold, due to the larger $e^+e^- \to W^+W^-$ cross section and to the increase in the boost of the W bosons.

The invariant mass distribution of the events satisfying all cuts is shown in figure 6. The single W events are concentrated in the mass range 60-100 GeV/c^2, consistent with a mass resolution of approximately 10 GeV/c^2. In this signal region (cut F) we observe 2 events at $\sqrt{s} = 161$ GeV and 2 events at $\sqrt{s} = 172$ GeV, with an expectation of 1.08 and 1.39 events respectively. We give in appendix A the kinematical characteristics of these 4 candidates and their event displays. The signal is expected to account for 0.63 and 0.71 events at the two centre-of-mass energies. The remaining background is predicted to consist for approximately 50% of $W^+W^- \to q\overline{q}'\tau\overline{\nu}_\tau$ events, with the τ decay products having low momenta and thus being merged with the jets. Additional contributions to the background (approximately 35% of the total) are from $W^+W^- \to q\overline{q}'e\overline{\nu}_e$ and $W^+W^- \to q\overline{q}'\mu\overline{\nu}_\mu$ events with the lepton emitted in the forward direction, where the lepton identification criteria are less efficient. There is also a minor contribution from $e^+e^- \to q\overline{q}(\gamma)$ events (approximately 15%), while the contribution from all other background sources is negligible.

Selection efficiencies and the number of selected events in Monte Carlo and in the real data are summarised in tables 1 and 2 for $\sqrt{s} = 161$ and 172 GeV respectively.

We also study the variation of the signal efficiency as a function of the anomalous TGCs. This variation is taken into account when computing the limit on the cross section as a function of the anomalous couplings. The selection efficiency for Monte Carlo events generated with TGC values different from the Standard Model values is given in figure 7. The variation of the selection efficiency is due to the change in the angular and energy distributions of the W boson produced.

Both the total σ_{tot} and the differential cross section at any point of the phase space have a quadratic dependence on the anomalous couplings. As a consequence the accepted cross section σ_{acc} is a quadratic function of the TGCs. The exact dependence of the selection efficiency ε on κ_γ and of λ_γ is thus given by the ratio of two quadratic functions:

$$\varepsilon(\kappa_\gamma, \lambda_\gamma) \;=\; \frac{\sigma_{acc}}{\sigma_{tot}} \;=\; \frac{a_1 + a_2\,\kappa_\gamma + a_3\,{\kappa_\gamma}^2 + a_4\,\lambda_\gamma + a_5\,{\lambda_\gamma}^2 + a_6\,\kappa_\gamma\,\lambda_\gamma}{b_1 + b_2\,\kappa_\gamma + b_3\,{\kappa_\gamma}^2 + b_4\,\lambda_\gamma + b_5\,{\lambda_\gamma}^2 + b_6\,\kappa_\gamma\,\lambda_\gamma}$$

This fitted expression is used to extrapolate the selection efficiency to values of the TGCs different from those for which a Monte Carlo simulation is available.

4.2 Systematic errors

Systematic errors are estimated both for the accepted background cross section and for the signal selection efficiency. The luminosity is determined with a a statistical precision of 0.4% and a systematic error of 0.35% [31], and introduces an additional systematic error of 0.5%, common to the expected number of background and signal events.

The following sources of systematic errors on the accepted background cross section are taken into account:

1. The 0.06 GeV error on the centre-of-mass energies [7] causes a negligible error on the cross section for $e^+e^- \to q\overline{q}(\gamma)$ and a 0.25% error on the cross section for four–fermion final states (assuming these are dominated by the $e^+e^- \to W^+W^-$ process).

2. Different Monte Carlo samples are compared for $e^+e^- \to q\overline{q}(\gamma)$ and for the four–fermion backgrounds, without observing any significant difference. We take the statistical error of this test (12% and 8% at $\sqrt{s} = 161$ and 172 GeV respectively) as a systematic error. This error also includes the statistical error of the background Monte Carlo samples.

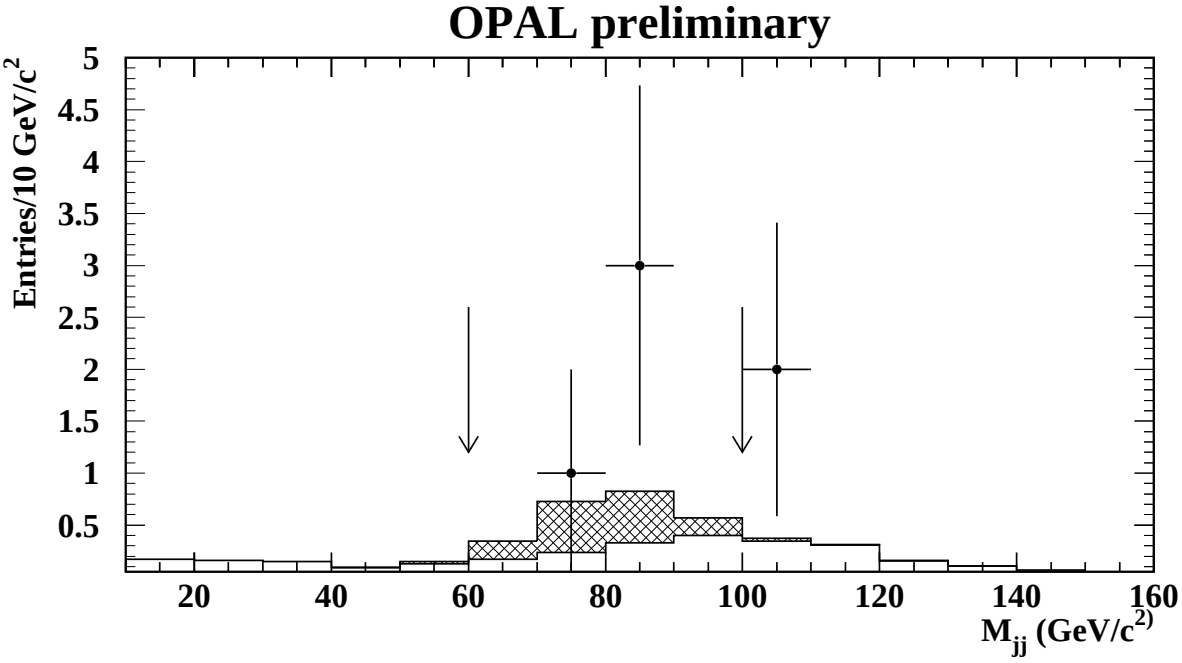

Figure 6: Distribution of the invariant mass of the two jet system. The open and the hatched histogram show respectively the distributions expected from the background and the single W signal Monte Carlo simulations. The full dots represent the 161 and 172 GeV data points. The arrows indicate the position of the cuts.

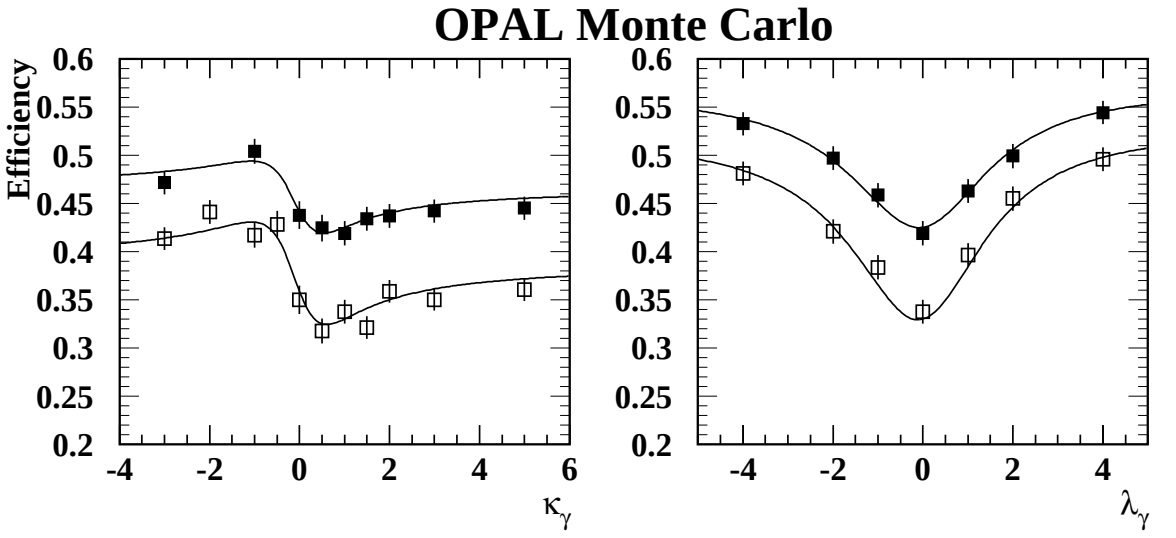

Figure 7: Selection efficiency for the simulated single W events as a function of the anomalous couplings κ_γ and λ_γ for $\sqrt{s} = 161$ GeV (full dots - ■) and for $\sqrt{s} = 172$ GeV (empty dots - □). The error bars indicate the Monte Carlo statistical error. The lines indicate the result of the fit to the Monte Carlo points.

161 GeV	$N_{\mathrm{background}}$				$\mathrm{We}\overline{\nu}_{\mathrm{e}}$		N_{data}
	$q\bar{q}$	4f	$\gamma\gamma$	Σ_{BG}	N	ϵ	
preselection	991 ± 3	26.7 ± 0.5	1474 ± 14	2492 ± 15	1.21 ± 0.02	(80.3±1.0)%	2440
cut A	823 ± 2	22.3 ± 0.5	1064 ± 12	1909 ± 12	1.13 ± 0.02	(74.8±1.1)%	1862
cut B	270 ± 1	8.7 ± 0.2	61 ± 3	340 ± 3	0.94 ± 0.02	(62.4±1.3)%	379
cut C	0.43 ± 0.06	2.4 ± 0.1	0.1 ± 0.1	2.9 ± 0.1	0.70 ± 0.02	(46.4±1.3)%	6
cut D	0.33 ± 0.05	1.11 ± 0.05	0.1 ± 0.1	1.54 ± 0.12	0.68 ± 0.02	(44.9±1.3)%	3
cut E	0.28 ± 0.04	0.99 ± 0.05	0	1.27 ± 0.06	0.66 ± 0.02	(44.1±1.3) %	3
cut F	0.06 ± 0.02	0.39 ± 0.03	0	0.45 ± 0.04	0.63 ± 0.02	(42.1±1.3)%	2

Table 1: Number of expected events and selection efficiencies at $\sqrt{s} = 161$ GeV. Errors shown are due to the Monte Carlo statistics only.

172 GeV	$N_{\mathrm{background}}$				$\mathrm{We}\overline{\nu}_{\mathrm{e}}$		N_{data}
	$q\bar{q}$	4f	$\gamma\gamma$	Σ_{BG}	N	ϵ	
preselection	854 ± 2	46.9 ± 0.6	1737 ± 18	2638 ± 19	1.74 ± 0.02	(81.1±1.0)%	2661
cut A	703 ± 2	40.2 ± 0.5	1145 ± 15	1888 ± 15	1.59 ± 0.02	(74.4±1.1)%	1971
cut B	226 ± 1	21.8 ± 0.2	59 ± 3	307 ± 3	1.36 ± 0.03	(63.7±1.3)%	329
cut C	0.38 ± 0.05	9.2 ± 0.1	0	9.6 ± 0.1	1.03 ± 0.03	(48.2±1.3)%	8
cut D	0.29 ± 0.05	2.68 ± 0.08	0	3.0 ± 0.1	0.96 ± 0.03	(45.0±1.3)%	4
cut E	0.15 ± 0.03	1.49 ± 0.04	0	1.66 ± 0.06	0.75 ± 0.03	(34.8±1.3)%	3
cut F	0.02 ± 0.01	0.66 ± 0.03	0	0.68 ± 0.04	0.71 ± 0.03	(32.9±1.2)%	2

Table 2: Number of expected events and selection efficiencies at $\sqrt{s} = 172$ GeV. Errors shown are due to the Monte Carlo statistics only.

3. Any difference between the predicted and observed distributions of the variables used in the selection procedure is a source of uncertainty in the accepted background cross section. We estimate the systematic error with the following procedure for each variable used in the selection. The distribution normalised to the data for each selection variable is used to reweight the background Monte Carlo samples in order to match its shape. The resulting change in the accepted cross section is taken as systematic error. For the hadronic final state we use two different data samples to obtain the reference distributions. The first one is enriched in $e^+e^- \to q\overline{q}(\gamma)$ events, and is obtained by applying cuts A and B of the selection described in section 4.1 and requiring the invariant mass of the jet pair to be larger than 50 GeV/c^2 to remove the two–photon events. The second reference sample is enriched in four–fermion events (reaching a fraction of 50% of the sample) by loosening the preselection cut to $y_{23} \leq 0.15$ and by requiring $\not{p}_t \geq 5.0$ GeV/c, $\phi_{\rm acop} \geq 5^\circ$, $|\cos\theta_{jj}| \leq 0.92$ and an invariant mass of the jet pair larger than 40 GeV/c^2. These distributions are not biased by the presence of the signal, given its small cross section. Comparable results are obtained with both methods, despite the limited data statistics available. The systematic error obtained with this procedure (7%) is dominated by the uncertainty on the modelling of the y_{23} variable (4.5%) and of the invariant mass of jet pairs (3.5%). Other major contributions come from the modelling of the missing momentum (2.5%) and of the angular distribution of the jets (2.5%).

The different contributions to the systematic error on the background prediction are summarised in table 3. Summing in quadrature all the different errors we obtain a total error of 14% and 11% on the background prediction at $\sqrt{s} = 161$ and 172 GeV respectively.

$\sqrt{s}$(GeV)	161	172
Luminosity	0.5%	
Beam energy	0.25%	
Different Monte Carlo samples	12%	8%
Detector response and background modelling	7%	
Total	14%	11%

Table 3: Systematic errors for the background description.

For the signal we take into account the following sources of systematic errors on the selection efficiency:

1. Monte Carlo statistics cause an uncertainty of 3% in the selection efficiency.

2. The difference between the two methods available in `grc4f` for generating the initial state radiation causes an uncertainty of 5% in the accepted cross section.

3. The mean charged track and electromagnetic calorimeter cluster multiplicity of the Monte Carlo signal sample agree within errors with those measured in the data using a sample of $W^+W^- \to q\overline{q}'\ell\overline{\nu}_\ell$ decays identified as in [30]. Variation of the mean charged track multiplicity of one unit and of the electromagnetic cluster multiplicity of two units result in a systematic uncertainty of 0.7%.

4. The cut on the jet recombination parameter $y_{23} \leq 0.03$ introduces an inefficiency of (8.7 ± 1.0)%. When $W^+W^- \to q\overline{q}'\ell\overline{\nu}_\ell$ decays identified as in [30] are considered, removing the lepton from the event, this cut introduces an inefficiency of (7.8 ± 4.0)%. As the results are compatible, the statistical uncertainty of this check is taken as systematic error.

5. Additional energy deposits in the forward calorimeters due to beam halo may cause a reduction of the signal selection efficiency. We therefore shift the energy measured in the forward calorimeters

by the difference between the average deposits in the data and in the simulation. We take the change in the selection efficiency of the single W signal (2%) as a systematic error.

6. Differences between data and Monte Carlo simulations in the reconstruction of the jet angles are investigated using Z^0 data collected in 1996 prior to high energy runs. The simulation describes correctly the resolution on the jet angles, although a shift in the polar angle of less than 0.5° is observed. The effect of changing the polar angle of the jets alone or of the reconstructed two jet system by this quantity introduces an uncertainty on the signal selection efficiency of 2%. Applying the same shift to the azimuthal angle (and thus to the acoplanarity of the jet pair) results in a systematic uncertainty of 1%.

7. Analogously the Monte Carlo simulation is found to reproduce correctly the distribution of the missing transverse momentum, as shown in figure 3b. If the missing transverse momentum and the missing energy are shifted in the signal Monte Carlo for the difference in the mean values of distributions between data and background Monte Carlo samples (respectively by 0.5 GeV/c and by 1.0 GeV), the selection efficiency of the signal changes by 2.5% which we take as systematic error.

8. The efficiency of the cut on the transverse momentum of the tracks identified as leptons is studied using $W^+W^- \to q\overline{q}'q\overline{q}'$ decays selected as in [30], ignoring possible differences in the angular distribution and in the spectra of W bosons. This cut removes $(8.5 \pm 3.8)\%$ of the events, whereas the single W Monte Carlo gives an inefficiency of $(5.0 \pm 0.7)\%$. Taking into account that in the first case two W bosons contribute to the inefficiency, the two results are compatible, and we take the statistical error of the data efficiency (1.9%) as systematic error.

9. The effect of the cut on the invariant mass of the jet pair can be checked using radiative returns to the Z^0 peak. The position of the peak is shifted in the data by -0.6 ± 1.0 GeV/c^2 relative to that of the Monte Carlo, and the mass resolution is a factor (1.11 ± 0.11) worse in the data than in the Monte Carlo, due to inaccuracies of the simulation of the response of the hadronic calorimeter. If the shift is applied in the Monte Carlo, and the smearing of the W mass peak due to the reconstruction is worsened by the factor derived above, the selection efficiency of the single W signal changes by 2.5%, which we take as systematic error.

10. The systematic error due to the uncertainty on the trigger efficiency is negligible due to the high track multiplicity requirement.

11. Uncertainties related to the fragmentation process are estimated to be smaller than 2% by comparing the difference between the selection efficiencies obtained by fragmenting the same four-fermion final states with JETSET and with HERWIG.

The different contributions to the systematic error on the signal selection efficiency are summarised in table 4. Summing them in quadrature the systematic error on the selection efficiency of the hadronic channel is 9%.

5 Leptonic final states ($\ell\nu_\ell e\overline{\nu}_e$)

5.1 Event selection

Electronic and muonic decays of the W boson produced in the $e^+e^- \to W^+e^-\overline{\nu}_e$ reaction are characterised by a single track in the detector. We select events in which only one good track with momentum larger than 5 GeV/c is found, allowing at most four additional bad tracks. To select good tracks and clusters we use the criteria defined in [32]. The total visible energy is required to be larger than 5%

Luminosity	0.5%
Monte Carlo statistics	3%
Initial state radiation	5%
Track and cluster multiplicity	0.7%
y_{23} cut	4%
E_{GC},E_{FD},E_{SW}	2%
Jet directions	2.2%
$\not{p}_t$, $\not{E}$	2.5%
Lepton identification	1.9%
Invariant mass resolution	2.5%
Fragmentation	2%
Total	9%

Table 4: Systematic errors for the signal.

of the centre-of-mass energy. Cosmic rays are efficiently vetoed by rejecting events with more than 5 clusters in the hadronic calorimeter.

Background from lepton pairs where one of the tracks is not reconstructed is rejected if additional detector activity is found in the direction of the missing momentum vector. We define the angle ψ as the difference between the azimuthal angles of the missing momentum vector and of the direction of additional track segments or energy clusters. Events are rejected if one of the following conditions is satisfied by the track segments or the energy clusters contained within the cone $\cos\psi > 0.9$ (cut 1):

- a candidate track is found in the muon detector,
- an electromagnetic calorimeter cluster above a threshold of 100 MeV in the barrel and 250 MeV in the endcap is found, or
- an energy deposit larger than 1 GeV is found in the hadronic calorimeter.

The numbers of events selected in the data, the Monte Carlo prediction and the signal selection efficiency are given in tables 5 and 6 for $\sqrt{s} = 161$ and 172 GeV respectively.

An isolation criterion is then applied to the lepton candidate track. The distribution of the sum of energy of the electromagnetic calorimeter clusters which are outside a cone of 450 mrad half–opening angle centered on the lepton track candidate is shown in figure 8. Electron pairs and two–photon events are rejected by requiring that at most 5 GeV are deposited in the electromagnetic calorimeter outside this isolation cone (cut 2).

The background from two–photon processes is suppressed further by demanding the sum of the energy deposits in the forward calorimeters (GC, FD and SW) to be smaller than 5 GeV (cut 3), and a missing transverse momentum larger than 20 GeV/c (cut 4). The distribution of the missing transverse momentum after cut 3 is shown in figure 9.

We then require the good track to satisfy lepton identification criteria, otherwise the event is rejected (cut 5). Lepton identification is performed applying the following cuts:

- Electrons are identified requiring $0.5 < E_{em}/E_{vis} < 2.0$, where E_{em} and E_{vis} are the energy deposited in the electromagnetic calorimeter and the total visible energy respectively.
- Tracks giving energy deposits smaller than 0.2 and 2 GeV in the electromagnetic and hadronic calorimeter respectively, and matching track segments in the hadronic calorimeter and/or the muon chambers are identified as muons.

The distribution of the polar angle of the single–electron and single–muon candidates after these cuts are shown in figure 10. The single W signal is selected requiring that the lepton is emitted at large polar angles: we require $|\cos\theta| < 0.8$ for electrons and $|\cos\theta| < 0.9$ for muons (cut 6).

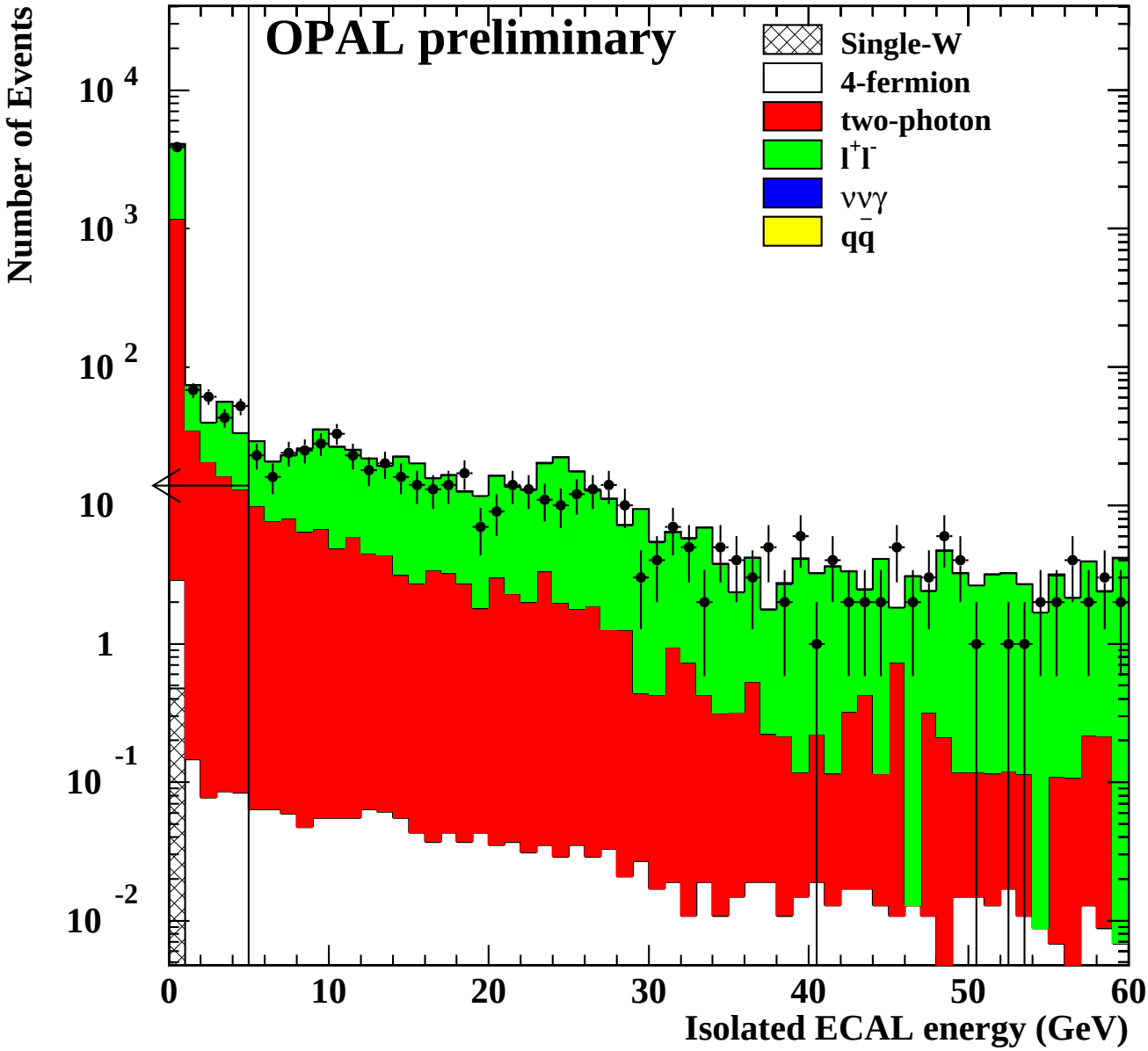

Figure 8: Distribution of the total energy in the electromagnetic calorimeter outside a cone of 450 mrad half–opening angle centered on the lepton track candidate for $\sqrt{s} = 172$ GeV, after cut 1. Data are shown as points. The histogram shows the expected background distribution from different background samples. The expected contribution from the $e^+e^- \to W^+e^-\overline{\nu}_e$ reaction followed by electronic or muonic decay of the W boson is shown in the hatched histogram. The arrow indicates the position of the cut.

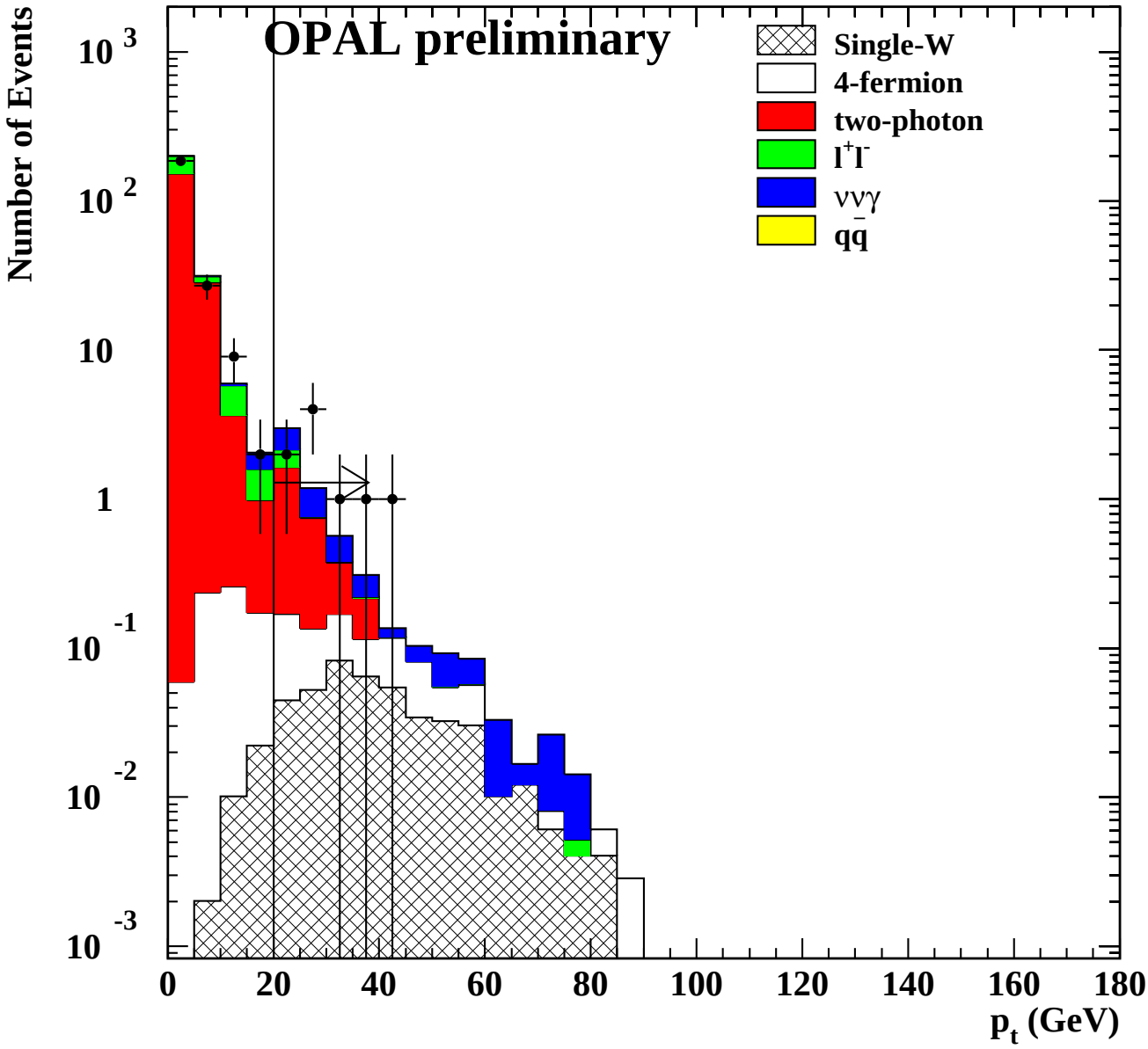

Figure 9: Missing transverse momentum distribution after cuts 1–3 for the data taken at $\sqrt{s}$ = 172 GeV (points with error bars).The histogram shows the expected background distribution from different background samples. The expected contribution from the $e^+e^- \to W^+e^-\overline{\nu}_e$ reaction followed by electronic or muonic decay of the W boson is shown in the hatched histogram. The arrow indicates the position of the cut.

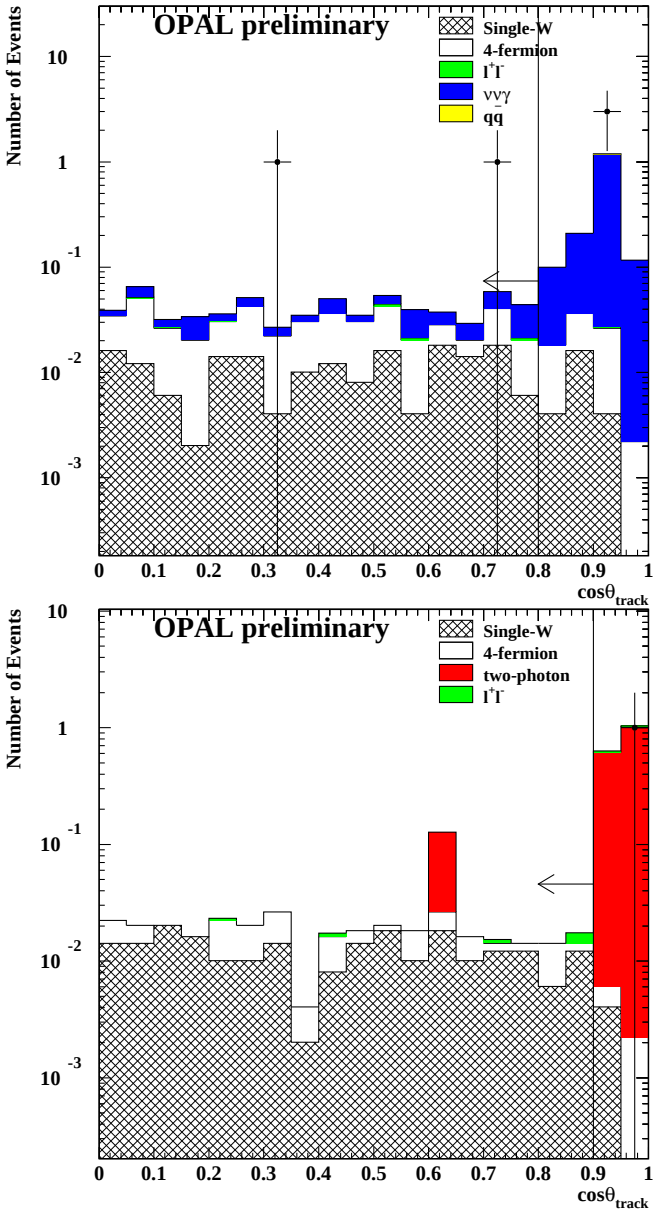

Figure 10: Polar angle distribution after cuts 1–5 for single–electron final states (top) and for single–muon final states (bottom) for the 172 GeV data. The histogram shows the expected background distribution from different background samples. The expected contribution from the $e^+e^- \to W^+e^-\overline{\nu}_e$ reaction followed by electronic or muonic decay of the W boson is shown in the hatched histogram. The arrow indicates the position of the cut.

161 GeV	$N_{\text{background}}$					$\text{We}\overline{\nu}_{\text{e}}$		N_{data}
	$\gamma\gamma$	$\ell^+\ell^-$	$\nu\overline{\nu}\gamma$	4f	Σ_{BG}	N	ϵ	
cut 1	1274 ± 14	3641 ± 36	6.0 ± 0.2	1.11 ± 0.06	4922 ± 39	0.425 ± 0.005	(94.3±1.2)%	4752
cut 2	1173 ± 14	3002 ± 34	3.0 ± 0.1	0.99 ± 0.06	4179 ± 37	0.423 ± 0.005	(93.9±1.2)%	4101
cut 3	183 ± 5	61 ± 5	2.4 ± 0.1	0.66 ± 0.05	247 ± 7	0.407 ± 0.007	(90.3±1.5)%	224
cut 4	2.5 ± 0.5	0.26 ± 0.20	0.95 ± 0.08	0.26 ± 0.03	4.0 ± 0.6	0.369 ± 0.009	(81.8±2.0)%	2
	Single electron final state							
cut 5	0	0.017 ± 0.005	0.92 ± 0.08	0.17 ± 0.03	1.11 ± 0.09	0.184 ± 0.004	(79.9±1.7)%	1
cut 6	0	0.013 ± 0.004	0.12 ± 0.03	0.15 ± 0.02	0.28 ± 0.04	0.157 ± 0.005	(68.4±2.0)%	0
	Single muon final state							
cut 5	2.2 ± 0.5	0.039 ± 0.008	0	0.08 ± 0.02	2.3 ± 0.5	0.176 ± 0.003	(79.7±1.1)%	0
cut 6	0.1 ± 0.1	0.005 ± 0.002	0	0.08 ± 0.02	0.19 ± 0.11	0.170 ± 0.003	(77.0±1.2)%	0

Table 5: Number of expected events and selection efficiencies at $\sqrt{s} = 161$ GeV. Errors shown are due to Monte Carlo statistics only.

172 GeV	$N_{\text{background}}$					$\text{We}\overline{\nu}_{\text{e}}$		N_{data}
	$\gamma\gamma$	$\ell^+\ell^-$	$\nu\overline{\nu}\gamma$	4f	Σ_{BG}	N	ϵ	
cut 1	1366 ± 12	3608 ± 39	6.3 ± 0.3	4.3 ± 0.1	4985 ± 41	0.573 ± 0.018	(94.0±3.0)%	4725
cut 2	1259 ± 11	2999 ± 36	3.5 ± 0.2	2.8 ± 0.1	4264 ± 38	0.573 ± 0.018	(94.0±3.0)%	4107
cut 3	187 ± 4	55 ± 5	2.6 ± 0.1	1.20 ± 0.05	246 ± 6	0.559 ± 0.021	(91.7±3.5)%	232
cut 4	2.4 ± 0.5	0.55 ± 0.50	1.72 ± 0.09	0.51 ± 0.03	5.2 ± 0.7	0.518 ± 0.028	(84.9±4.5)%	9
	Single electron final state							
cut 5	0	0.009 ± 0.003	1.69 ± 0.09	0.38 ± 0.03	2.08 ± 0.09	0.263 ± 0.010	(84.6±3.3)%	5
cut 6	0	0.008 ± 0.003	0.16 ± 0.03	0.32 ± 0.02	0.49 ± 0.04	0.232 ± 0.013	(74.4±4.0)%	2
	Single muon final state							
cut 5	1.7 ± 0.4	0.042 ± 0.007	0	0.10 ± 0.01	1.8 ± 0.4	0.247 ± 0.010	(83.0±3.2)%	1
cut 6	0.1 ± 0.1	0.006 ± 0.003	0	0.10 ± 0.01	0.21 ± 0.12	0.243 ± 0.010	(81.5±3.3)%	0

Table 6: Number of expected events and selection efficiencies at $\sqrt{s} = 172$ GeV. Errors shown are due to Monte Carlo statistics only.

The expected number of signal and background events and the signal selection efficiency are given in tables 5 and 6 for $\sqrt{s} = 161$ and 172 GeV respectively. Two candidates are found in the single–electron channel for $\sqrt{s} = 172$ GeV and none at $\sqrt{s} = 161$ GeV. No candidates are found in the single–muon channel. The kinematical properties and the event displays of the two candidates are given in Appendix A. The first of these candidates, shown in figure 16 is most probably a radiative return to the Z^0, followed by the decay of the Z^0 into a pair of neutrinos and the conversion of the photon in one of the silicon planes. The positron coming from the conversion can be seen as a curling track that is not reconstructed by the track finding program. To avoid possible biases introduced by rejecting events with a visual scanning procedure, this event is considered as a candidate when computing the limit on the anomalous couplings.

5.2 Systematic errors

The background systematic error due to uncertainties in the modelling of the variables used in the event selection is estimated in a manner similar to that employed in section 4.2. The Monte Carlo reproduces well the distributions of the variables used in the selection observed in the data. However, to estimate a systematic error due to possible differences in these distributions, each variable of the Monte Carlo is shifted by its expected measurement accuracy or by the difference in average values between data and simulation. The resulting difference in the accepted background cross section is then assigned as the systematic error. In total the contribution from uncertainties in the modelling of the variables used in the event selection amounts to 5%. Additional systematic errors which we consider are:

1. The photon conversion probability which is studied using multi–photon events. The 10% difference between the data and the Monte Carlo simulation is taken as systematic error. This translates into a systematic error of 4% in the background estimate for the single–electron channel.

2. The dominant error on the accepted background cross section which comes from the limited Monte Carlo statistics. This error is 12% and 8% for the single–electron channel at $\sqrt{s} = 161$ and 172 GeV, and 58% for the single–muon channel for both centre-of-mass energies.

The systematic error on the signal selection efficiency due to the detector response is estimated as for the background to be 5%. The effect of additional background hits in the forward calorimeters is studied using random beam crossing events, and affect the selection efficiency by at most 2%, which we conservatively take as the systematic error. The trigger is assumed to be fully efficient for the single–electron channel, because of the requirement of an high energy deposit in the electromagnetic calorimeter. For the single–muon channel we explicitly study the trigger inefficiency using muon–pair events. The trigger is found to be fully efficient within the angular range relevant for this analysis. We take the statistical error of this study (5%) as a conservative systematic error of the trigger efficiency. The Monte Carlo statistics and differences in the accepted cross sections between the two methods available in `grc4f` for simulating the initial state radiation contribute to the systematic error of 4.5% and 6% respectively. The total systematic uncertainty on the selection efficiency is therefore 9% and 11% for the single–electron and single–muon final states respectively.

6 Limit on the anomalous couplings

The cross section for single W production has a quadratic dependence on the anomalous couplings κ_γ and λ_γ. We obtain limits on these parameters by performing a maximum likelihood fit to the number of observed events. We perform the fit assuming that only the single W cross section varies if the anomalous couplings assume values different from the Standard Model predictions. Given that the background of the hadronic channel is dominated by the reaction $e^+e^- \to W^+W^-$ whose cross

section also depends on the anomalous couplings, it would be preferable to perform a fit where both the signal and the background cross sections are allowed to vary with the TGCs. However this would then require that assumptions are made about the relations between the γWW and Z^0WW couplings. Hence we prefer to perform the fit allowing only the signal cross section to vary with κ_γ and λ_γ. We therefore obtain a conservative limit on these parameters, since the enhancement of the cross section is assigned only to the signal, instead of being shared by both the signal and the background.

To take into account the systematic errors on both the accepted background cross section and the signal detection efficiency, we maximise the following likelihood with respect to the anomalous couplings κ_γ and λ_γ:

$$\mathcal{L} \;=\; \sum_i \log \iint \mathcal{G}(f^i_{sign.}, \sigma^i_{sign.})\, \mathcal{G}(f^i_{backg.}, \sigma^i_{backg.})\, \mathcal{P}(N^i, n^i)\, df^i_{sign.}\, df^i_{backg.}$$

where the Poisson distribution to observe N events in one of the data samples (electron, muons or hadrons, for two different centre-of-mass energies) is expressed in terms of the expected number of signal events ($s = s(\kappa_\gamma, \lambda_\gamma)$) and background events (b) as:

$$\mathcal{P}(N, n) \;=\; \frac{(s\, f_{sign.} + b\, f_{backg.})^N}{N!}\, e^{-(s\, f_{sign.} + b\, f_{backg.})}.$$

The index i runs over the three different final states (electron, muon and hadrons) and two centre-of-mass energies ($\sqrt{s} = 161$ and 172 GeV). The multiplicative factors $f_{sign.}$ and $f_{backg.}$ introduced to take into account the systematic errors are allowed to vary from the central value of 1 with the gaussian distributions $\mathcal{G}$ of width σ. We introduce an independent width for each signal and background sample, neglecting possible correlations among the systematic errors.

From the difference of the log-likelihood curves with respect to the maxima, we derive the 95% confidence level exclusion region for the TGCs parameters κ_γ and λ_γ shown in figure 11. If only one of the anomalous couplings is left free in the fit, while the other assumes the value expected in the Standard Model we obtain the following 95% confidence level limits:

$$\begin{aligned} |\kappa_\gamma| &\leq 2.6, \\ |\lambda_\gamma| &\leq 3.1. \end{aligned}$$

7 Conclusions

We have selected a sample of 6 events at $\sqrt{s} = 161$ and 172 GeV which are all kinematically compatible with the $e^+e^- \to W^+e^-\overline{\nu}_e$ process followed by either hadronic or leptonic decay of the W boson, in agreement with the Standard Model predictions of 2.1 ± 0.1 events from the signal and 2.3 ± 0.2 events from backgrounds. From a fit of the cross section as a function of the anomalous couplings at the γWW vertex we derive the 95% confidence level limits $|\kappa_\gamma| \leq 2.6$ and $|\lambda_\gamma| \leq 3.1$. These limits are compared in table 7 to the those obtained by the L3 collaboration from the measurement of the single W cross section at $\sqrt{s} = 161$ and 172 GeV [33], and to those obtained by the CDF and D0 Collaborations measuring the Wγ production cross section in $p\overline{p}$ collisions at the Tevatron [34], [35]. Our limits are comparable to those obtained by the L3 Collaboration and a factor of 3 worse for κ_γ and a factor of 10 worse for λ_γ than those obtained from $p\overline{p}$ collisions.

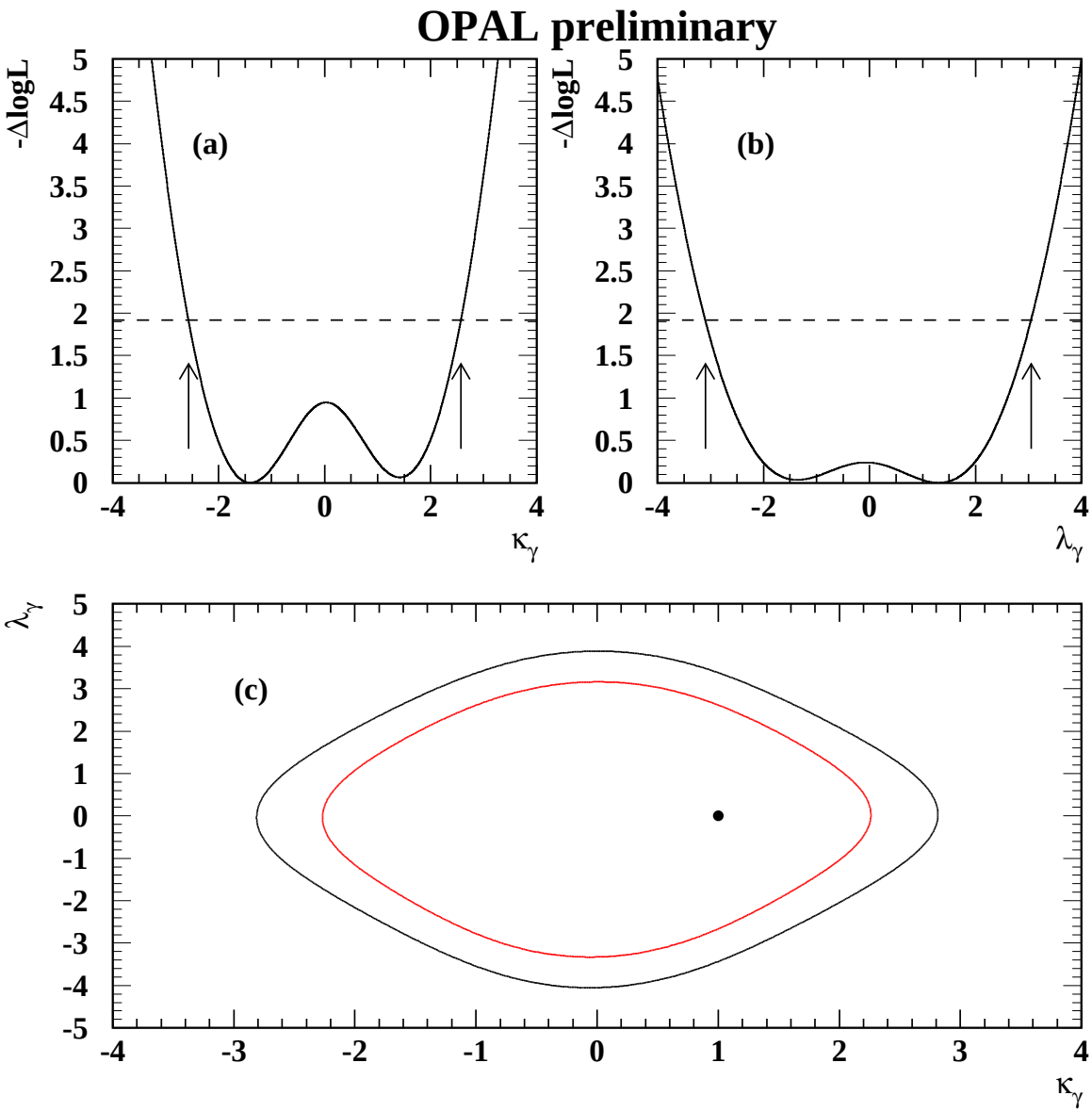

Figure 11: Difference of the log–likelihood relative to the maximum found by the fit as a function of κ_γ for $\lambda_\gamma = 0$ (a) and λ_γ for $\kappa_\gamma = 1$ (b). The arrows indicate the position of the 95% confidence level exclusion limits. The two lines in (c) indicate respectively the exclusion regions at the 95% and 70% confidence level in the parameter space (κ_γ,λ_γ). The point shows the expected value of the γWW couplings in the Standard Model.

Single W production in e^+e^- collisions		
This note	$-2.6 \leq \kappa_\gamma \leq 2.6$	$-3.1 \leq \lambda_\gamma \leq 3.1$
L3 [33]	$-2.6 \leq \kappa_\gamma \leq 2.5$	$-3.6 \leq \lambda_\gamma \leq 3.6$
Wγ production in $p\overline{p}$ collisions		
CDF [34]	$-1.3 \leq \kappa_\gamma \leq 3.2$	$-0.7 \leq \lambda_\gamma \leq 0.7$
D0 [35]	$0.02 \leq \kappa_\gamma \leq 1.01$	$-0.33 \leq \lambda_\gamma \leq 0.31$

Table 7: Comparison of recent results on the γWW anomalous couplings.

References

[1] T. Tsukamoto and Y. Kurihara, Phys. Lett. **B389** (1996) 162.

[2] Physics at LEP2, Edited by G. Altarelli, T. Sjostrand and F. Zwirner, Report on the LEP2 Workshop 1995, CERN 96-01, Vol. 1, p. 525.

[3] The OPAL Collaboration, K. Ackerstaff *et al.*, Phys. Lett. **B397** (1997) 147;
The OPAL Collaboration, *Measurement of triple gauge boson couplings from* W^+W^- *production at* $\sqrt{s} = 172$ *GeV*, OPAL Physics Note PN287, 17^{th} march 1997.

[4] J. Fujimoto *et al.*, Comp. Phys. Comm. **100** (1997) 128.

[5] The OPAL Collaboration, K. Ahmet *et al.*, Nucl. Instr. Meth. **A305** (1991) 275;
P.P. Allport *et al.*, Nucl. Instr. Meth. **A324** (1993) 34, Nucl. Instr. Meth. **A346** (1994) 476.

[6] B.E. Anderson *et al.*, IEEE Transactions on Nuclear Science, **41** (1994) 845.

[7] LEP Energy Working Group, LEP energy calibration in 1996, LEP Energy Group/97-01, 20^{th} march 1997.

[8] T. Sjöstrand, Comp. Phys. Comm. **82** (1994) 74.

[9] K. Hagiwara, H. Iwasaki, A. Miyamoto, H. Murayama and D. Zeppenfeld, Nucl. Phys. **B365** (1994) 544.

[10] A.E. Kuraev and V.S. Fadin, Sov. J. Nucl. Phys. **41** (1985) 466.

[11] Y. Kurihara, J. Fujimoto, T. Munehisa and Y. Shimizu, Prog. Theor. Phys. **96** (1996) 1223.

[12] J. Fujimoto, private communication.

[13] F.A. Berends, R. Pittau and R. Kleiss, Comp. Phys. Comm. **85** (1995) 437.

[14] J. Hilgart, R. Kleiss and F. Le Diberder, Comp. Phys. Comm. **75** (1993) 191.

[15] G. Marchesini *et al.*, Comp. Phys. Comm. **67** (1992) 465.

[16] S. Jadach *et al.*, Comp. Phys. Comm. **79** (1994) 503.

[17] S. Jadach *et al.*, Phys. Lett. **B390** (1997) 298.

[18] D. Karlen, Nucl. Phys. **B289** (1987) 23.

[19] G. Montagna, O. Nicrosini, F. Piccinini and L. Trentadue, Nucl. Phys. **B452** (1995) 161;
G. Montagna, O. Nicrosini and F. Piccinini, Comp. Phys. Comm. **98** (1996) 206.

[20] F.A. Berends and R. Kleiss, Nucl. Phys. **B186** (1981) 22.

[21] R. Engel and J. Ranft, Phys. Rev. **D54** (1996) 4244;
R. Engel, Zeit. Phys. **C66** (1995) 203.

[22] A. Buijs, W.G.J. Langeveld, M.H. Lehto and D.J. Miller, Comp. Phys. Comm. **79** (1994) 523.

[23] J.A.M. Vermaseren, Nucl. Phys. **B229** (1983) 347.

[24] J. Allison *et al.*, Nucl. Instr. Meth. **A317** (1992) 47.

[25] N. Brown and W.J. Stirling, Phys. Lett. **B252** (1990) 657;
S. Bethke, Z. Kunszt, D. Soper and W.J. Stirling, Nucl. Phys. **B370** (1992) 310;
S. Catani *et al.*, Phys. Lett. **B269** (1991) 432;
N. Brown and W.J. Stirling, Zeit. Phys. **C53** (1992) 629.

[26] The OPAL Collaboration, M.Z. Akrawy *et al.*, Phys. Lett. **B253** (1990) 511.

[27] The OPAL Collaboration, K. Ackerstaff *et al.*, Phys. Lett. **B389** (1996) 416.

[28] The OPAL Collaboration, R. Akers *et al.*, Zeit. Phys. **C70** (1996) 357.

[29] The OPAL Collaboration, R. Akers *et al.*, Zeit. Phys. **C65** (1995) 17.

[30] The OPAL Collaboration, *Measurement of the mass of the W boson and* $\mathrm{W^+W^-}$ *production and decay properties in* $\mathrm{e^+e^-}$ *collisions at* $\sqrt{s} = 172$ *GeV*, OPAL Physics Note PN301, 25^{th} july 1997.

[31] The OPAL Collaboration, R. Akers *et al.*, *Tests of the standard and constraints on new physics from measurement of fermion pair production at 130-172* GeV *at LEP*, preprint CERN-PPE/97-101, submitted to Zeit. Phys. C.

[32] The OPAL Collaboration, G. Alexander *et al.*, Phys. Lett. **B377** (1996) 181.

[33] L3 Collaboration, M. Acciarri *et al.*, Phys. Lett. **B403** (1997) 168.

[34] CDF Collaboration, F. Abe *et al.*, Phys. Rev. Lett. **74** (1995) 1936.

[35] D0 Collaboration, S. Abachi *et al.*, Phys. Rev. Lett. **78** (1997) 3634.

Appendix A Properties of selected events

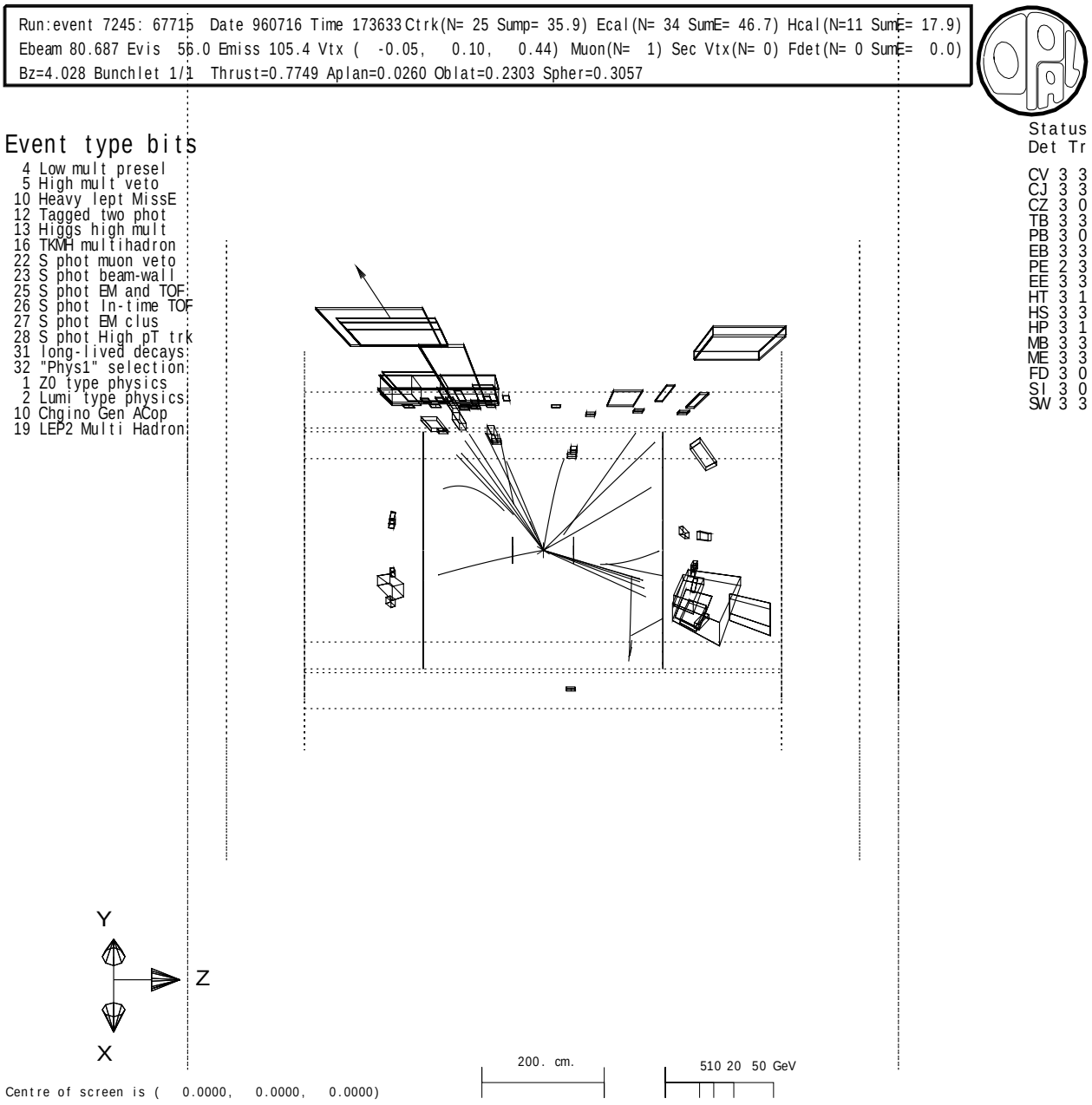

Figure 12: First selected event: run 7245, event 67715, $\sqrt{s} = 161$ GeV, $\not{p}_t = 32.2$ GeV/c, $\phi_{\mathrm{acop}} = 42.8°$, $E_{miss} = 36.5$ GeV, $M_{\mathrm{q\overline{q}'}} = 83.3$ GeV/c^2.

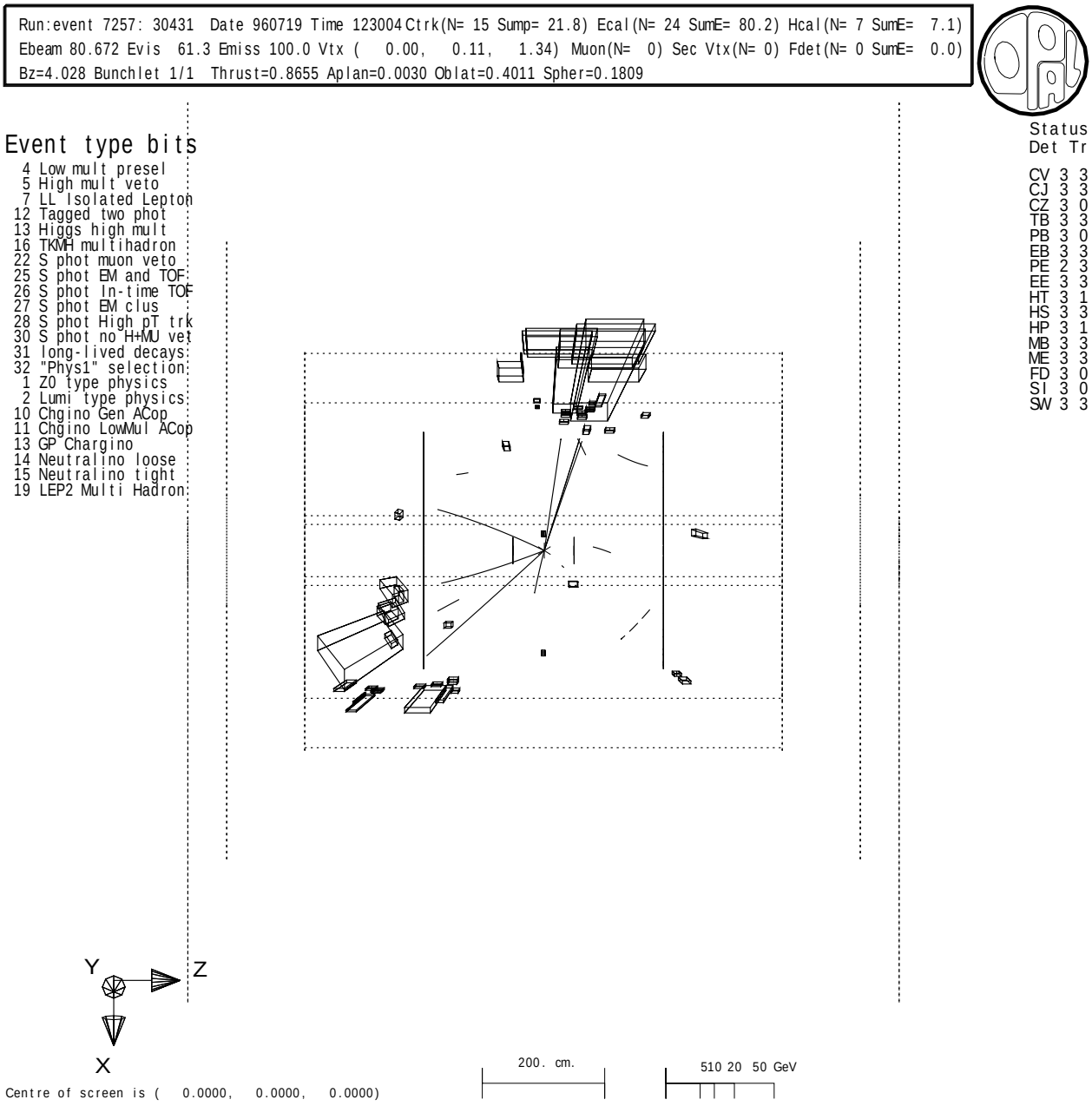

Figure 13: Second selected event: run 7257, event 30431, $\sqrt{s} = 161$ GeV, $\not{p}_t = 47.3$ GeV/c, $\phi_{\mathrm{acop}} = 48.8°$, $E_{miss} = 49.5$ GeV, $M_{\mathrm{q\overline{q}'}} = 79.8$ GeV/c^2.

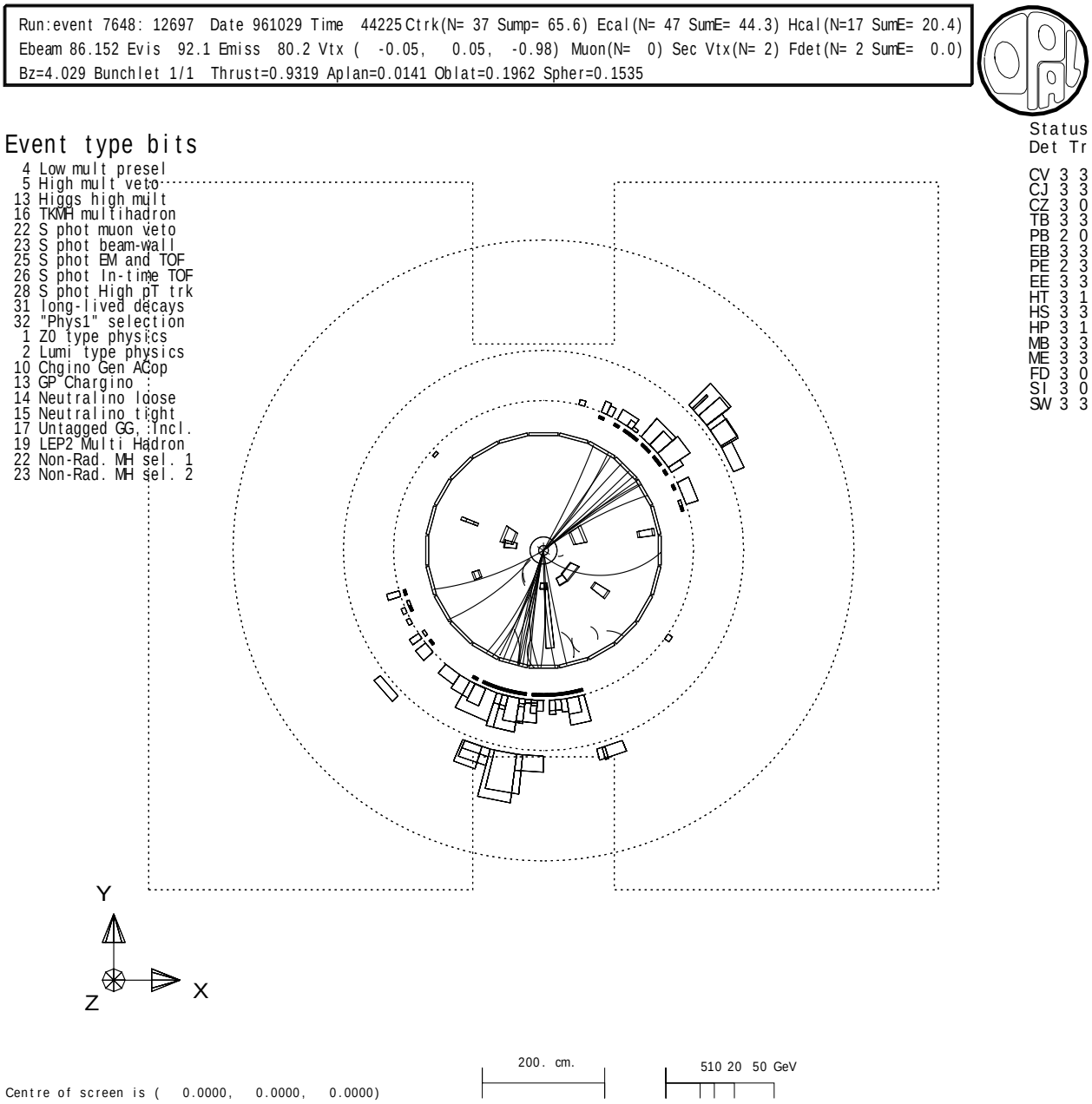

Figure 14: Third selected event: run 7648, event 12697, $\sqrt{s} = 172$ GeV, $\not{p}_t = 32.2$ GeV/c, $\phi_{\mathrm{acop}} = 33.4^\circ$, $E_{miss} = 35.6$ GeV, $M_{\mathrm{q\overline{q}'}} = 82.1$ GeV/c^2.

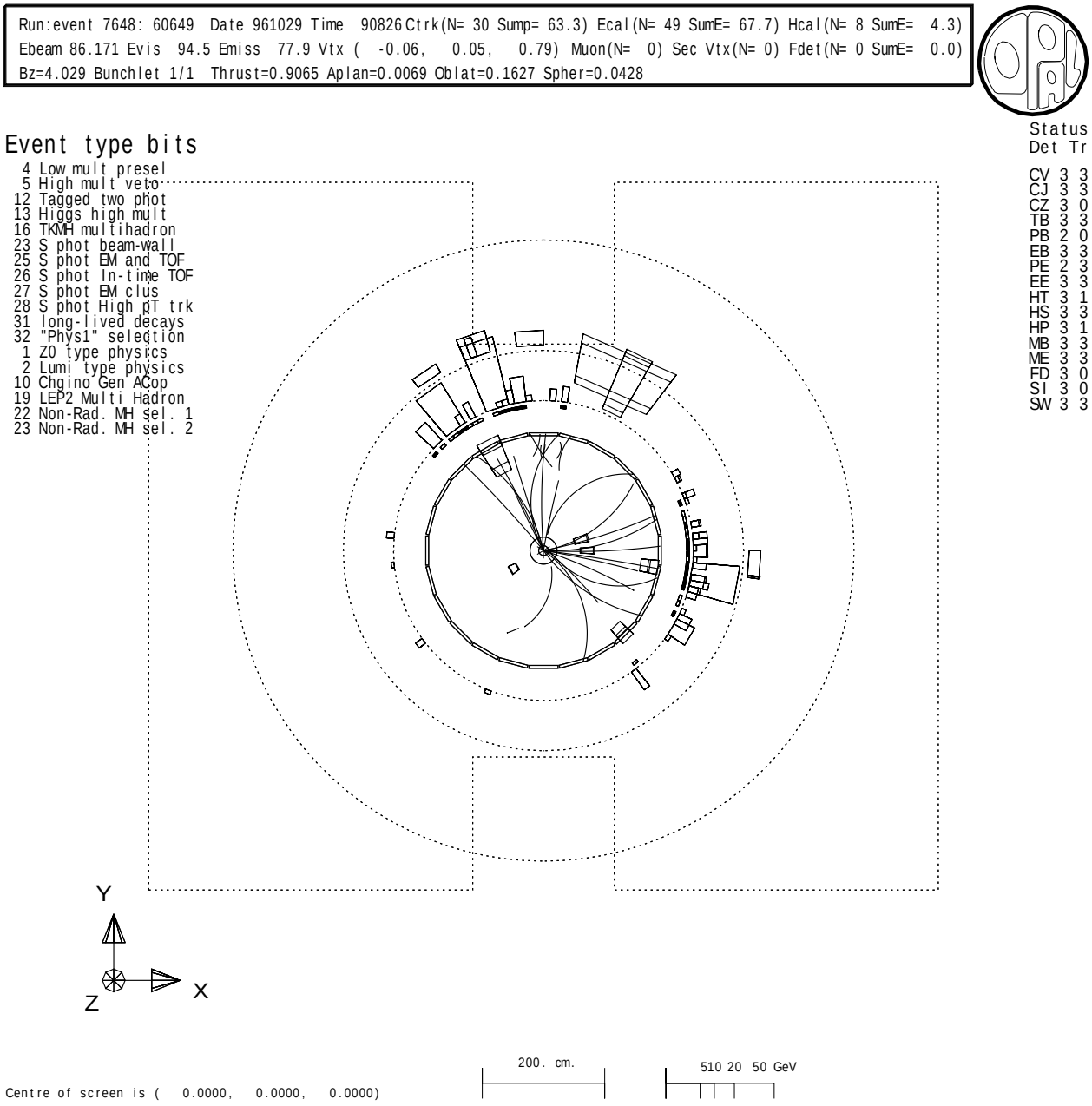

Figure 15: Fourth selected event: run 7648, event 60649, $\sqrt{s} = 172$ GeV, $\not{p}_t = 35.4$ GeV/c, $\phi_{\rm acop} = 59.0°$, $E_{miss} = 43.2$ GeV, $M_{\rm q\overline{q}'} = 84.7$ GeV/c^2.

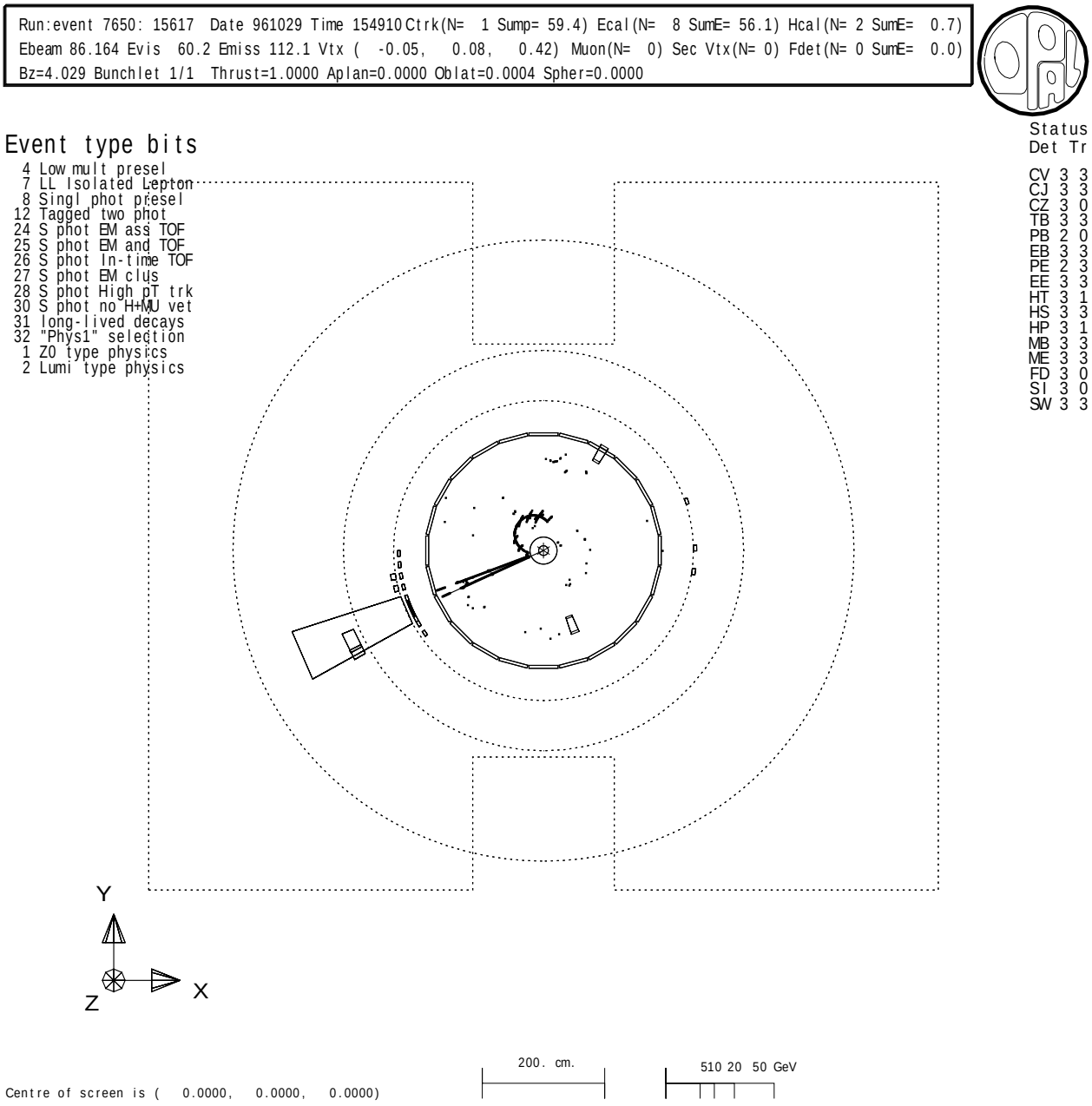

Figure 16: Fifth selected event: run 7650, event 15617, $\sqrt{s}$ = 172 GeV, $p_{t_{el}}$ =41.8 GeV/c, $\cos\theta_{el}$ = -0.71. All the central jet chamber hits with left/right ambiguity are shown. The curling track was not successfully reconstructed.

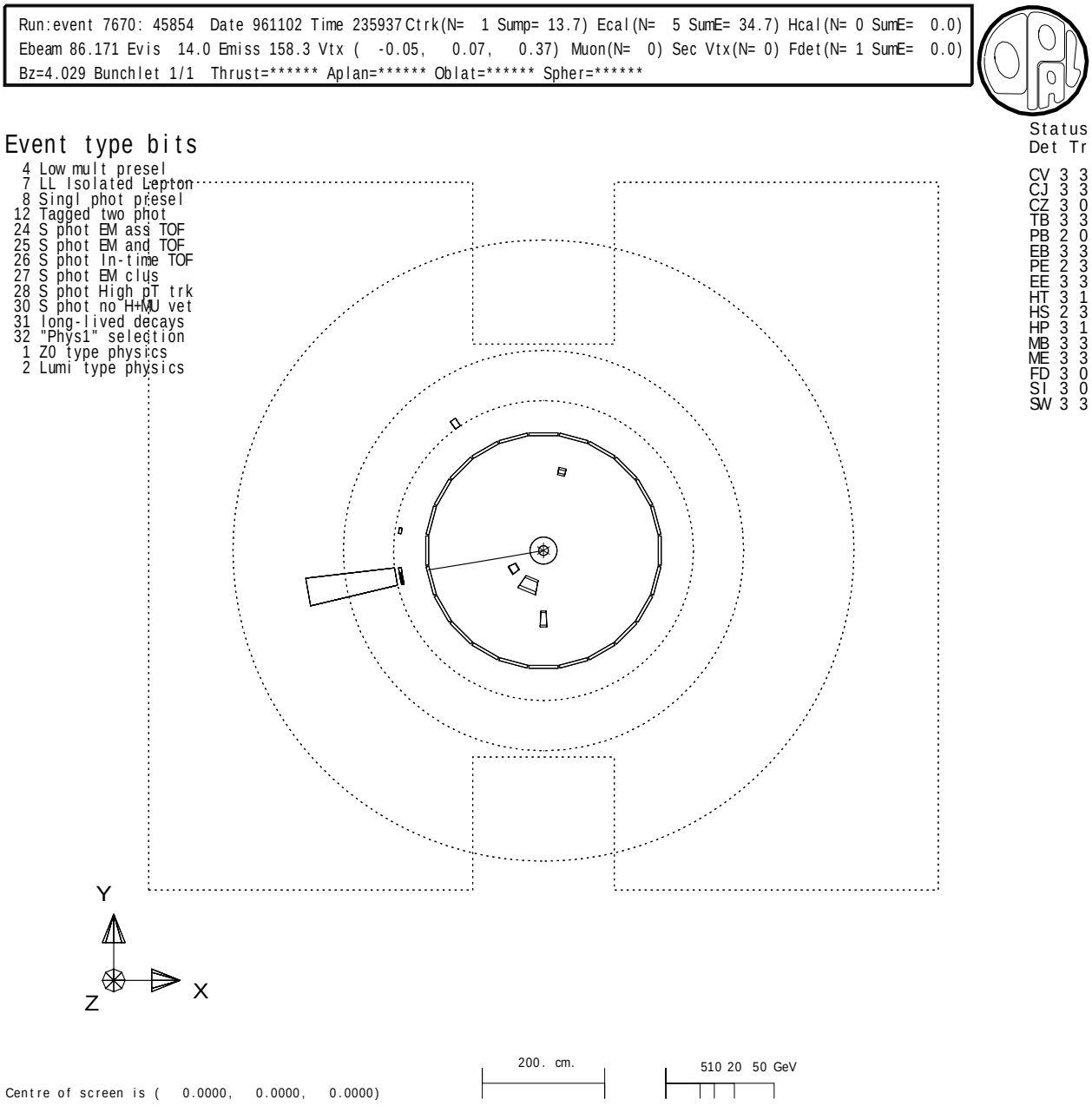

Figure 17: Sixth selected event: run 7670, event 45854, $\sqrt{s} = 172$ GeV, $p_{t_{el}} = 31.5$ GeV/c, $\cos\theta_{el} = 0.32$.